

**A low-cost modular underwater acoustic
communication system**

by

Charlene Xia

B.Sc., Massachusetts Institute of Technology (2017)

Submitted to the Program in Media Arts and Sciences,
School of Architecture and Planning in partial fulfillment of the
requirements for the degree of

Master of Science in Media Arts And Sciences

at the

MASSACHUSETTS INSTITUTE OF TECHNOLOGY

September 2020

© Massachusetts Institute of Technology 2020. All rights reserved.

Author
Program in Media Arts and Sciences,
August 3rd, 2020

Certified by.....
Joseph A. Paradiso
Professor of Media Arts and Sciences
Thesis Supervisor

Accepted by
Tod Machover
Academic Head, Program in Media Arts and Sciences

A low-cost modular underwater acoustic communication system

by

Charlene Xia

Submitted to the Program in Media Arts and Sciences,
on August 3rd, 2020, in partial fulfillment of the
requirements for the degree of
Master of Science In Media Arts and Sciences

Abstract

This thesis describes the design of a novel modular acoustic communication device for underwater wireless communication. The ocean plays a vital role in the global climate system and biosphere, providing a wealth of biodiversity and resources. Human exploitation, pollutants, and contaminants have already impacted the deepest trenches of the ocean. Yet most of this impact remains invisible - the depth and breadth of the ocean, the opacity of water to light, and the lack of mass-deployable ocean instrumentation, mean that current observations are wildly under sampled in space and time.

Even given suitable instruments, a major challenge remains: how to get the data home. Given the opacity of sea water to radio, and the complexity and expense of underwater cabling, audio communication is in many ways the low hanging fruit. Unfortunately, most commercial audio communication systems are both extremely expensive and more powerful than needed for many, if not most, monitoring requirements. They are also proprietary, a frustrating barrier to development of novel devices. As a result, these off-the-shelf systems are ill-suited to the global multi-scale instrumentation challenges of the future.

In what follows we document the design, development, and testing of a low-cost, high-efficiency, modular, and fully open-sourced acoustic communication system. This system is specifically intended for mass deployment, with particular emphasis on standardized hardware and software interfaces. Crucially, this design prioritizes cost and simplicity over performance - as such, this system does not aim to replace the current crop of commercially available systems, but rather to provide a new kind of tool specifically for scalable deployments of low-cost instruments. Functionally, the system is composed of three core modules: a power management unit; a central processing unit; and a family of interchangeable acoustic transceiver units operating across a spectrum of transmission frequencies. The resulting design should be of valuable use to the scientific community, environmental agencies, citizen scientists, and anyone who needs to transport low-bandwidth data through the ocean at extremely low cost.

Thesis Supervisor: Joseph A. Paradiso
Title: Professor of Media Arts and Sciences

**A low-cost modular underwater acoustic communication
system**

by
Charlene Xia

This thesis has been reviewed and approved by the following committee
members:

Professor Joseph A. Paradiso
Chairman, Thesis Committee
Professor of Media Arts and Sciences

Professor Allan Adams.....
Thesis Supervisor
Principle Investigator, Future Ocean Lab

Shah Selbe
Member, Thesis Committee
Founder of Conservify

Contents

1	Introduction	11
1.1	The need for large scale ocean observation	11
1.1.1	Survey of Existing Technology	13
2	Hardware Design	17
2.1	Overview	17
2.2	Acoustic Transducer	19
2.2.1	Piezoelectric Ceramic Transducer	22
2.2.2	Mechanical Properties	26
2.2.3	Electrical Properties Characterization	27
2.2.4	Making an underwater Piezoceramic Transducer	29
2.3	Transmission Board	35
2.3.1	Power Amplifier Design	36
2.3.2	Impedance Matching Circuit	41
2.3.3	Power Converter Circuit	42
2.3.4	Board Connector	44
2.4	Receiver Board	46
2.4.1	Instrumentation Amplifier	46
2.4.2	Autogain Control Circuit	52
2.4.3	Board Connector	54
2.5	Power Management	55
2.6	Processor Board	56
2.7	Housing Design	59

2.8	Modularity	62
3	Digital Design	63
3.1	Overview	63
3.2	Frequency Modulation	64
3.2.1	BFSK Encoding	64
3.2.2	BFSK Decoding	65
3.3	Phase Modulation	70
3.3.1	DBPSK Encoding	70
3.3.2	DBPSK Decoding	71
4	System Test and Evaluation	75
4.1	Overview	75
4.2	Water Tank Test	75
4.2.1	BFSK	76
4.2.2	DBPSK	80
4.3	Power Analysis	83
4.4	Bill of Material	85
5	Next Steps	89
5.1	Hardware Consideration	89
5.2	Software Considerations	90
5.3	Design Variations	91
5.4	Biological and Environmental Considerations	95
A	Bill of Material	96

Chapter 1

Introduction

This thesis contains the design and preliminary evaluation of OpenModem, a low-cost underwater acoustic modem. The current design is set at 25kHz carrier frequency. The OpenModem is tested in a constrained space to >99% accuracy at 200 bits per second. The simulated maximum performance is 2000 bits per second. The battery life is estimated to be around 80 hours at low operation (1 TX RX operations per hour) mode. The physical housing is designed to be pressure safe and waterproof up to 1500m. The bill of material at low volume (<10) is under \$200, at high volume (>1000) is under \$90. The electronic, and mechanical designs, results of simulation and testing, and plans for future improvements are all detailed in this document. Beyond the information included in this thesis, the OpenModem project is currently ongoing and updated on the Future Ocean Lab online PubPub page: <https://futureocean.pubpub.org/>.

1.1 The need for large scale ocean observation

Our ocean is a highly connected, and dynamic environment. It is full of life and resource, interconnected with our land and our atmosphere. Yet we know very little about the current health of our ocean. Contaminants, pollutants, and human exploitation have already impacted the global ocean to an unknown extent. Deep-ocean biodiversity loss and climate-induced shifts are already occurring in areas [1].

Due to the vastness, the ocean is undersampled and under observed spatially and temporally. Most of our ocean remains unseen, unquantified, completely unknown [2]. There is now a coalition of international deep-ocean stakeholders from science, management, government and industry for waters to support a globally integrated network of systems to observe the ocean [3]. A global qualitative observation of our ocean will lead to a deeper understanding of the condition of our ocean and ultimately guide our actions to protect and conserve our ocean.

Wireless underwater communication has a wide range of applications such as habitat monitoring systems, environmental research, autonomous underwater vehicle operation to name a few. Scalable sensing and monitoring technology will provide a more complete view of the the Ocean's spatial and temporal complexities. It is an essential infrastructure element needed to support sensors observation and remote vehicle operation. The main advantages of wireless communication over wired tethered communication are ease of installation and maintenance, location accessibility and flexibility in network planning. Efficient wireless underwater communication is fundamental and critical for scalable observation. A low-cost underwater modem will contribute greatly to an effective underwater communication network. An adequate modem requires moderate transmission ranges (<500m), low data rates, and a wide range of deployment depths (<1500m). Acoustic communication is the preferred physical layer for underwater wireless communication. A low frequency acoustic wave, such as a whale song, can easily travel over kilometers. There are many variables to consider and navigate in modem design. Devices for ocean deployment face challenges of longevity, pressure and corrosion resistance, power and deployment cost.

The OpenModem project is focused on developing a quality modem with adequate performance and design with scalability and adaptability in mind. Cutting down the cost per device means we can send 100 devices underwater instead of 10. 100 devices deployment can drastically change the scope and types of ocean research. OpenModem is designed to tackle the fundamental sampling problem faced in ocean researching. The increase in the volume and quality of data collected will significantly increase researcher's capacity to observe and study ocean phenomena. In addition,

by breaking down the existing cost and technology barriers, we can foster a global community of users from different sectors.

Here we present OpenModem, a scalable underwater acoustic communication design. We are achieving scalability through two means, low cost and modularity. The estimated bill of material of the device at scale at less than \$90, magnitude lower than the cheapest off the shelf acoustic modem. A low-cost point means larger user groups and larger deployment. Modularity and open architecture offer adaptivity for different user needs and applications, from short distance high bit-rate to longer distance lower bit-rate.

The hardware components of the acoustic modem are mainly composed of a microprocessor, transmission board, receiving board, power management circuit, battery, the piezoelectric transducer, and pressure housing. The piezoelectric transducer acts as an underwater microphone and speaker. The transmission board is composed of a power amplifier and an impedance matching network for the specific piezoelectric. The receiving board is composed of a voltage-controlled gain amplifier with an anti-aliasing filter. The microprocessor is modulating and demodulating the signal along with implementing the network protocol. The components are either housed in a pressure and corrosion resistant housing or pressure compensated and potted in polyurethane. The design is adaptable to different frequencies (25kHz, 250kHz, 2MHz) based on their applications and environments.

1.1.1 Survey of Existing Technology

Commercial underwater acoustic modems are traditionally targeted for the sub-sea oil and gas industry and defense industry. Due to the demanding criteria of reliability and performance for these industries, the price of commercial modems is set at a premium thousands of dollars. Additional hardware, such as pressure-resistant open safe connectors needed to be used in conjunction with the modems also cost in the thousands.

The Link Quest Sound Link underwater acoustic modem uses a proprietary broadband acoustic spread spectrum technology to achieve a high data rate with a low bit

error rate. The system features advanced hybrid modulation, channel equalization, and environmental adaptation [4]. AquaSent uses OFEM for high performance data transfer, with a proprietary algorithm, and high speed digital processor [5]. Evo Logics underwater communication modem based on sweep spread technology, offers a series of different transmission rates and transmission distance modems [6] The Aquacomm underwater modem has a smaller form factor [7]. Teledyne Benthos also offers a selection of acoustic modems at different transmission rates and distances [8]. The Micron Data Modem is designed for underwater vehicle control system, small size and lightweight with lower data rate, 40bps, and transmission distance 500m horizontal [9]. High end underwater modems, such as Linkquest, Benthos, and DSPComm modems all cost more than \$8000. Lower end modems still cost between \$1500 to \$3000. Zia Et Al. composed a detailed classifications and analyses of commercial modems [10].

In summary, commercial modems are designed to satisfy the high-performance industry requirements. Due to the high cost barrier, commercial acoustic modems are inaccessible to civil groups, limiting for the scientific community and environmental organizations, and impractical for large scale deployment. Also, commercial devices offer very little documentation on software adjustment for the user. Each company has its proprietary network scheme. Existing devices offered may satisfy specific application scenarios, however, they lack the capability of switching between operation modes and open architectural support for adaptation. Also, many of them requires additional expensive proprietary hardware for connection. These and other technical barriers further precludes many groups of users from ocean exploration.

Academically developed modems are designed to test the comparative performance of modulation schemes, bandwidth utilization, power efficiency and low-cost design. MIT Sea Grant's rModem and CSAIL's AquaNodes offers a variable degree of reconfigurability and reprogrammability in physical implementation and network protocols. The MIT rModem implemented quadrature phase shift keying and reported 550b/s at 12kHz central frequency [11]. MIT CSAIL's AquaNodes, implemented a frequency shift modulation scheme at 30kHz with data rates of 330b/s up to 400m [12]. UCSD's

Low-Cost Modem is specifically designed to be both software defined and low cost for a specific low-cost piezoelectric transducer. The resulting system is performing at 200b/s FSK modulation in 32-38kHz band with an estimated cost of 600 dollars at scale [13].

WHOI's MicroModem exploits multichannel PSK and lower rate frequency-hopped FSK modulation. The high-rate MicroModem is a preliminary implementation of a software-defined modem with BPSK modulation and demodulation on FPGA, with carrier frequency of 800kHz reportedly achieved a bit rate of 80kb/s [14]. University of Valencia's Low-Power ITACA Modem pushed for a very-low-power modem, with carrier frequency at 85kHz transmitting a coherent FSK scheme with data reported at 1kb/s [15]. University of Calabria and their commercial spinoff SppliCon's SeaModem, a low-cost, sub 600 dollars, underwater acoustic modem with both physical and network layer reprogrammability, runs in the 25-35 kHz band [16].

Most of the modems mentioned above are research prototypes that are not commercially available. Cost-focused academic modems are still too expensive to be scalable and accessible. Academic research acoustic modems are designed in house and made to fit the design specs needed at the lab. The usage scenarios of research modems are usually contained in the originating academic institute. Most academic research acoustic modems are not accessible for users outside of their academic group. Documentations are often opaque to a beginner or even the modest DIY hacker. Users are often working with heterogeneous systems, with various hardware and software formats. Currently, if a researcher wants to add a wireless remote control for their underwater vehicle, they can either buy a commercial acoustic modem, spending thousands of dollars, or design and make their own wireless modem from scratch. The high cost barrier precludes the wide utilization of commercial products in environmentally focused and research applications.

Chapter 2

Hardware Design

2.1 Overview

The OpenModem design is focused on striking a balance between performance, cost, and usability. The current system is composed of a piezoelectric transducer connected through the housing endcap. The pressure housing holds the transmission and receiving circuit boards, the processing board, battery management unit, and an external pressure-safe connector. Frequency and phase modulation layers are implemented. OpenModem is designed to be modular as a stand alone transmitter, receiver or transceiver.

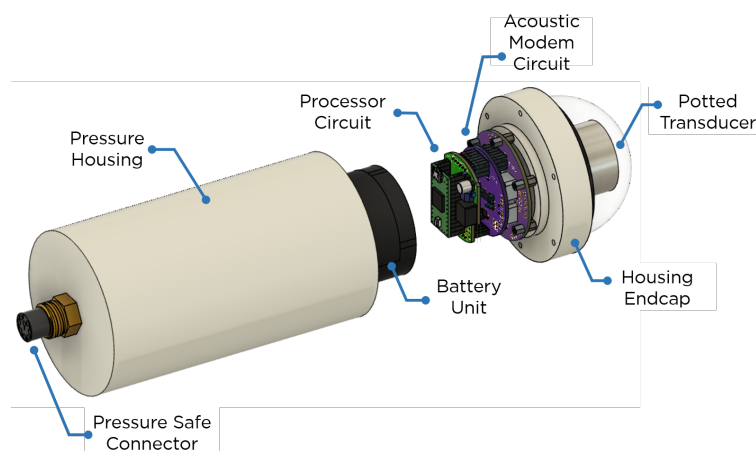


Figure 2-1: Diagram of core OpenModem components

OpenModem battery pack is composed of four 3.7V Li-ion 18650 batteries in

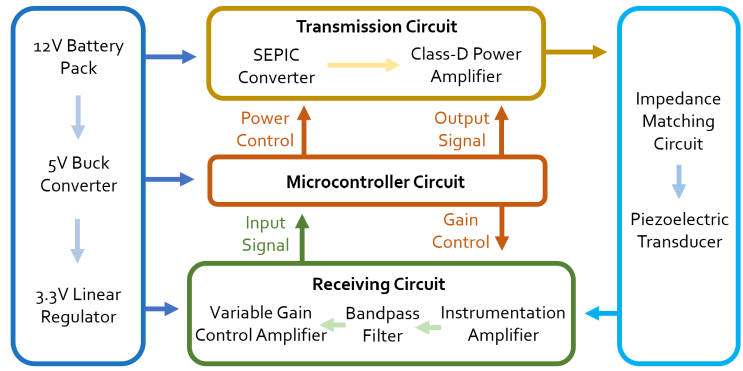


Figure 2-2: Block diagram of the OpenModem electronic circuit

series with a battery protection circuit that is powering the entire system. The piezoelectric transducer is both the acoustic speaker, transmitter and the acoustic microphone, receiver. The transmission circuit amplifies the output signal from the controller circuit to the piezoelectric transducer. The received signal from the piezoelectric transducer is amplified and filtered then decoded by the controller circuit. The controller circuit adjusts the transmission power level and receiver amplification gain based on the environmental condition, noise level, and power consumption.

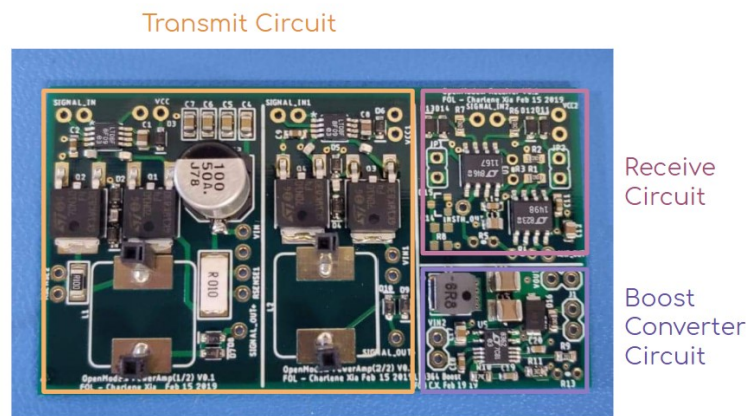


Figure 2-3: OpenModem analog electronic board Version 1, microcontroller board not included

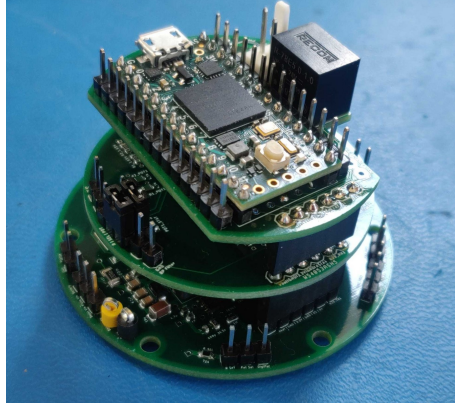


Figure 2-4: OpenModem electronic stack Version 2 - From top to bottom, processor and power management board, receiver board and transmission board.

2.2 Acoustic Transducer

Radio frequency, optical, and acoustic wave for underwater wireless communication all have their own advantages and constraints. Radio frequency ($<300\text{GHz}$) electromagnetic waves offer high data rate, however, are affected by high attenuation in water, which requires high transmission power and large antennae to compensate. The attenuation is due to the high salt content thus high conductivity of the sea water. Optical waves, between 400nm to 700nm , can be used to achieve ultra-high-data-rate communication, but are rapidly scattered and absorbed in turbid water, only reliable for short-distance links. For our purpose and application, acoustic waves remain the optimal solution for a balance of attaining significant distance, low cost, and high data rate as the communication method underwater. [17].

The ocean is a complicated inhomogeneous acoustic medium. The speed (v) of an acoustic signal is approximately 1500 m/s and varies depending on salinity (S), temperature (T), and the depth (z). A simplified estimation is shown below.

$$v = 1449.2 + 4.6T - 0.055T^2 + 0.00029T^3 + (1.34 - 0.010T)(S - 35) + 0.016z$$

Wavelength is calculated from the following formula. For water borne sound, v is the speed of sound underwater and f is the frequency of the signal.

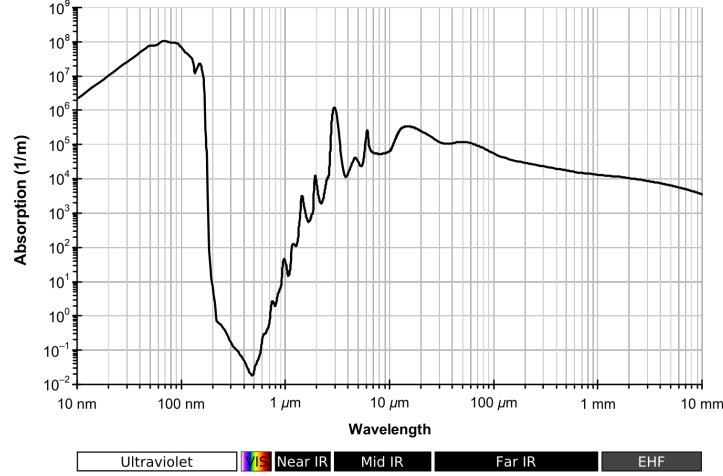


Figure 2-5: Optical absorption spectrum of electromagnetic wave in liquid water

$$\lambda = v/f$$

As the acoustic wave travels across the ocean, the wave decays due to scattering and absorption. The attenuation of sound waves between 3kHz to 0.5Mhz, β can be estimated and modeled by the following empirical formula, where S is salinity, P is hydrostatic pressure (kg/cm^2), f is frequency (kHz), and T is the temperature (Celsius). f_T is the relaxation frequency (kHz) of boric acid and magnesium sulfate in the ocean, which contributes to the deviation of ocean acoustic attenuation from freshwater.

$$\beta = 8.68 \times 10^3 \left(\frac{SAf_T f^2}{f_t^2 + f^2} + \frac{Bf^2}{f_T} \right) (1 - 6.54 \times 10^{-4} P) [dB/km]$$

$$f_T == 21.9 * 10^{6-1520/(T+273)}$$

$$A = 2.34 \times 10^{-6}$$

$$B = 3.38 \times 10^{-6}$$

The ocean is extremely variable. As currents, internal waves, and small scale

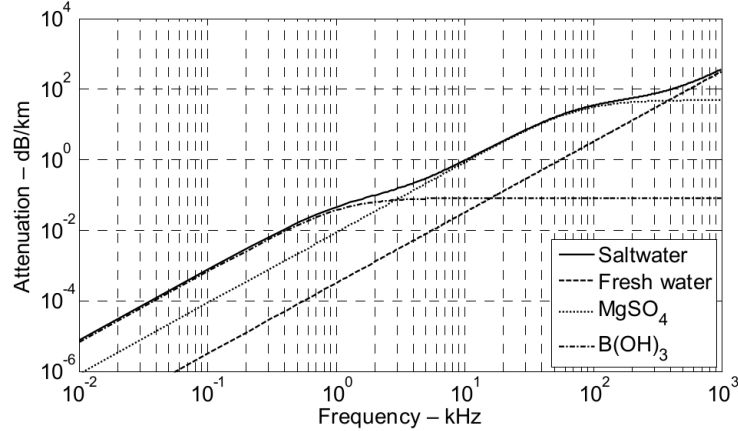


Figure 2-6: Acoustic absorption (dB/km) for fresh water and saltwater, plotted for water temperature of 10°C, atmospheric pressure of one atmosphere (surface), salinity of 35 pro mille, and pH value of 7.8.

turbulence cause spatial and temporal fluctuations in acoustic propagation. Environmental noise comes from four main sources: turbulence, shipping, waves, and thermal noise. There also exist acoustic scattering from the ocean surface, plus sound from air bubbles and assemblages of small marine animals. Underwater in a channel with unknown features, there exist multiple paths from the transmitter to the receiver. Multipath can be caused by wave reflection at boundaries, and sound refraction.

Depending on the deployment method, the relative motion between the transmitter and receiver can cause additional signal distortion, manifesting as the Doppler effect, a frequency shift of the signal waveform. Vertical transmission is difficult due to multipath propagation, while horizontal channels exhibit less distortion. The ocean acoustic channel has a lot of variation and unpredictability [18].

The current version of the OpenModem is using a 25kHz cylindrical piezoelectric transducer. Lower frequency signals can travel farther at the trade-off of lower baud rate and higher noise and interference. Higher frequency signals can have a higher baud rate, better noise and interference performance, at the trade-off of transmission distance. We picked 25kHz to start with because it is a good trade-off between baud rate and transmission distance.

2.2.1 Piezoelectric Ceramic Transducer

We want a relatively cost and power-efficient speaker and microphone underwater. The speaker should be acoustically impedance matched to water. The principle idea of impedance matching, will come up over and over again in many different forms in this project. Acoustic impedance is the ratio of acoustic pressure to flow. It is an important parameter to optimize for efficient acoustic energy transfer between two media. Acoustic impedance, Z is defined by the formula below, where ρ is the density of the material, and v is the acoustic velocity. The product of density and speed of sound in water is about 5000 times higher than this product in air. Therefore the acoustic impedance of water much greater than air.

$$Z = \rho v$$

At the boundary of two acoustic impedances, we get reflection and transmission. When the incident wave reaches the boundary of two mismatching impedance, most of the power in the incident wave is reflected, rather than transmitted. Imagine a rope tied to a brick wall. If you swing the rope up once, the wave will travel through the rope to the wall and get reflected back but downward. If the rope is free at the end, the wave will also get reflected back. Because of the impedance mismatch, most of the energy you put in to swing the rope gets reflected back to you. The paper-thin speaker is impedance matched in the air but not in water. If the two impedances are matched there is no reflection and the wave is fully transmitted. Transmission (t) and reflection (r) coefficient formulas are shown below [19].

$$t = \frac{2Z_2}{Z_1 + Z_2}$$
$$r = \frac{Z_2 - Z_1}{Z_2 + Z_1}$$

Piezoelectric ceramic is a better impedance-matched material as an underwater acoustic transducers. A piezoelectric material will produce a proportional electric polarization change when a mechanical deformation is applied. Conversely, when an

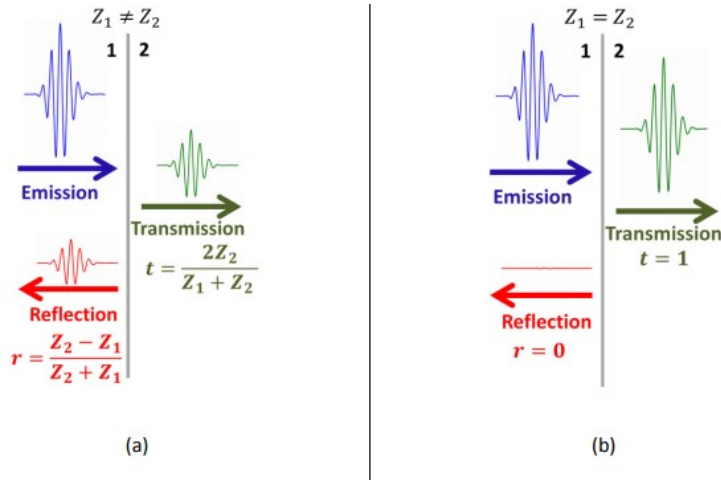


Figure 2-7: Schematic of sound wave propagation through two interfaces. [20]

electric voltage is applied across the piezoelectric material, the material will deform proportionally. When we applied an alternating voltage, for example, a 22kHz sine wave, across the piezoelectric material, it will mechanically vibrate at 22kHz like a speaker. When the piezoelectric material gets hit by a 22kHz pressure wave, it will create a corresponding 22kHz electrical potential across its electrode acting as a microphone.

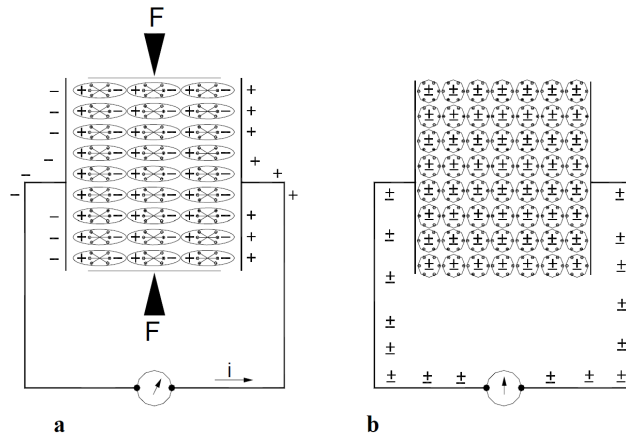


Figure 2-8: Schematic of piezoelectric effect: when an external force is applied on a piezoelectric material a neutralizing current is generated

There is a variety of different piezoelectric materials, ranging from natural and synthetic single quartz crystals to piezoelectric ceramics, and thin films. For our application, an underwater acoustic transducer, the qualities we are looking for are

high piezoelectric sensitivity, high mechanical strength, and low production cost. Lead-Zirconite-Titanate mixed ceramics (PZT) are the most common commercially-available piezoelectric ceramics. PZT exhibits very high piezoelectric coupling coefficients. We mainly focused on PZT. There are also other piezoelectric material such as barium titanate (BaTiO) and piezoelectric ceramic-polymer composites that is used in underwater acoustic transducer applications. However, they are not explored in this design iteration due to their high cost, specialized manufacturing method and limited commercial availability. Sonars have been made out of PVDF and piezoelectric copolymer, but higher-coefficient materials like PZT tends to dominate [21]. The drawbacks of PZT ceramics are instability at high temperatures and high variation in temperature. For our underwater application, the ocean's temperature variation is well within the limit of PZT operation. There are two main types of PZT, soft and hard, which are further separated into different standard Navy types. Soft piezoelectric is characterized by wider signal bandwidth and lower mechanical quality factors than hard piezoelectric.

There are assorted material properties that we need to consider when deciding on the types of PZT. The volume of change when a piezoelectric material is subject to an electric field, is characterized by the piezoelectric coefficients. The piezoelectric coefficients are the ratios of polarization when stress is applied. Another important factor is the electromechanical coupling factor, k , which is a measure of the effectiveness of the piezoelectric material in converting input electrical energy into mechanical energy. The piezoceramic and water acoustic impedances are still mismatched. Higher transmission can be achieved by inserting between the two regions an intermediate impedance. We will be doing just that by potting the piezoceramic. Different applications require different needs and trade-offs between bandwidth and power transfer [22]. The piezoelectric material has two resonant frequencies: mechanical and electrical.

Piezoelectric transducers operate best at resonance. The mechanical resonance frequency is dependent on the dimensions of the ceramic and to a lesser extent the matching layer. For the current version of the OpenModem, we are using a 25kHz

Piezo ceramic cylinder SMC3831T25111 from STEMiNC. The reported mechanical resonant frequency is around 25kHz with radial mode vibration. The piezo ceramic is a modified Navy Type I piezo ceramic with high mechanical Q-factor, low mechanical loss, and narrow signal bandwidth. It strikes a good balance for transmission and receiving purposes [23].



Figure 2-9: STEMiNC SMC3831T25111 25kHz piezoelectric ceramic cylinder

PIEZO MATERIAL PROPERTIES

PROPERTY	UNIT	SYMBOL	SM111	SM112	SM118	SM121	SM211	SM311	SM410	SM411	SM422	SM412	SM510	SM511	SM512	SM523	SM701	SM702	
EQUIVALENCE			Modif. PZT-4	N/A	PZT-8	PZT-4	N/A	PZT-5H	PZT-5J	PZT-5J	Modif. PZT-5	PZT-5A	Modif. PZT-5	BaTiO3	N/A	N/A	Actuators	Acoustic Wave	
			Modif. Navy Type I	N/A	Navy Type III	Navy Type I	N/A	Navy Type VI	Navy Type V	Navy Type V	N/A	Navy Type II	N/A	BaTiO3	N/A	N/A	N/A	N/A	N/A
Electromechanical coupling coefficient		K _p	0.58	0.59	0.51	0.54	0.67	0.65	0.64	0.64	0.64	0.63	0.65	0.34	0.60	0.64	0.65	0.06	
		K _t	0.45	0.46	0.40	0.43	0.35	0.37	0.45	0.45	0.48	0.42	0.50	0.32	0.50	0.50			0.49
		K ₃₁	0.34	0.35	0.30	0.32	0.41	0.38	0.36	0.37	0.36	0.35	0.38	0.196	0.35	0.36	0.38		
Frequency constant	Hz • m	N _p	2200	2150	2340	2290	1940	1980	2030	2060	1990	2080	2000				1960	1900	
		N _t	2070	2050	2090	2080	1920	1950	2050	2000	2040	2080	2250				2150	1900	2200
		N ₃₁	1680	1600	1700	1690	1410	1450	1460	1500	1460	1560					1750		
Piezoelectric constant	×10 ⁻¹² m/v	d ₃₃	320	360	250	300	650	600	500	500	500	450	450	160	400	550	640	50	
		d ₃₁	-140	-155	-100	-130	-320	-270	-210	-210	-210	-190	-210	30	170	-227	-410		
		g ₃₃	25	24.7	25.6	26.4	13.6	19.4	23.3	24.2	23.3	25.6		14.3	28	23.3	16		
Elastic Constant	×10 ¹⁰ N/m ²	g ₃₁	-11.0	-10.6	-12.5	-12.9	-6.7	-9.2	-10.3	-10.4	-10.3	-12.6		5.4	12	-9.9			
		Y ₃₃	7.3	7.2	7.4	7.3	5.1	5.3	5.6	5.4	5.6	5.6		119					
		Y ₁₁	8.6	8.4	8.7	8.6	6.2	7.2	6.5	7.4	6.5	7.6			16.6	57.5			
Mechanical Quality Factor	-----	Q _m	1800	1600	1200	1000	60	80	60	85	60	100	70	1200	85	75	65	800	
Dielectric Constant	@1KHz	e ^T _{33/e 0}	1400	1600	1100	1300	5400	3500	2000	2100	2200	1850	2100	1260	1600	2600	3800	250	
Dissipation Factor	%@1KHz	tan δ	0.4	0.6	0.2	0.4	3.0	2.5	2.0	2.0	1.2	2	0.5	2.0	2.0	0.4	1.5		
Curie Temperature	°C	T _c	320	320	300	320	165	220	320	290	320	260	115	350	270	180	250		
Density	g/cm ³	r	7.9	7.9	7.6	7.8	7.8	7.8	7.7	7.8	7.7	7.8	7.45	5.6	7.6	7.6	7.8	6.9	

Figure 2-10: Commercially available PZT material with properties options on STEMiNC [24]

2.2.2 Mechanical Properties

Common shapes for piezoceramic underwater transducers are rectangular, cylinders, and spheres. Cylinders and spheres shape offer a more Omni-direction transmission. The advantage of omni-direction transmission is more flexible positioning between modems. Transmission energy is not focused in a single direction but all directions, therefore there is spread loss. Cylindrical geometry suffers less spreading loss than spherical geometry. Cylinders are a common geometry used for hydrophones and underwater projector applications [25]. We chose a single piece of cylindrical piezoceramic as our transducer.

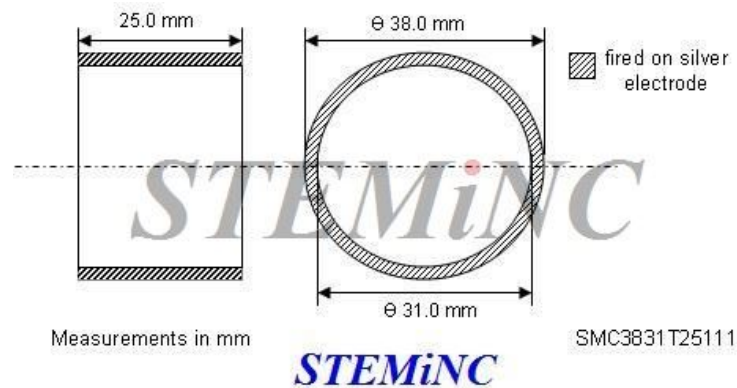


Figure 2-11: Dimension of 25kHz Piezoelectric ceramic cylinder by STEMiNC [24]

Another interesting mechanical configuration of a piezoelectric transducer is the tonpilz design, which is used commonly for Mid-range (1kHz - 100kHz) frequency projector designs. The basic design is composed of a stack of longitudinally poled piezoelectric ceramic rings is held in compression by a stress bolt between two metal masses, one at the back and one at the front. The mass at the back is designed to minimize acoustic radiation from the back of the transducer. The mass at the front is designed to be lightweight. While the tonpilz design isn't explored in the current version, it is worthwhile to dive deeper into it for future iteration.

2.2.3 Electrical Properties Characterization

We can model the electric impedance of the piezoelectric material, which is defined as the ratio between the applied voltage and the induced electric current. The electric impedance of the piezoelectric material changes when in-air, potted, or in-water. It is important to have a model of the piezoelectric transducer for the analysis of the transmission and receiver circuit.

The basic equivalent electric model of the piezoelectric is formed by two parallel branches, one mechanical branch which is formed by a $R_m L_m C_m$ and one static electrical branch formed by a capacitor C_0 . The current induced by the piezoelectric effect in the ceramic is represented by the RLC branch. C_0 is the electrical capacitance from the dielectric material placed between the inner silver coating and the outer silver coating. The current going through the mechanical RLC branch is proportional to the speed of the particle displacement. Therefore, near the RLC resonant frequency, which represents the mechanical resonant, current due to piezoelectric effect is at a maximum.

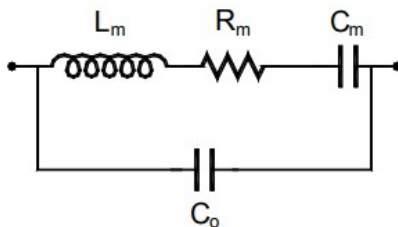


Figure 2-12: Butterworth Van-Dyke model of a piezoelectric resonator vibrating at frequencies near resonance

With an impedance analyzer, we measured the electrical impedance from 10Hz to 100kHz of the piezo ceramic in air and potted in water. Based on the Butterworth Van-Dyke model of piezoelectric resonance, with the impedance measurement of the piezo-ceramic, we can estimate the approximate value of R_m , L_m , C_m , and C_0 when the piezoceramic is vibrating near its first resonant frequency. Here ω_r is the resonant frequency. ω_a is the anti-resonant frequency. Z_{ω_r} is the measured impedance magnitude at the resonant frequency. Z_{ω_a} is the measured impedance magnitude at the anti-resonant frequency [26].

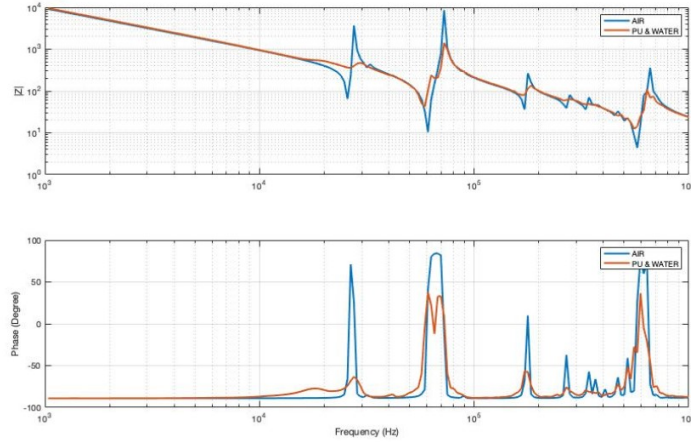


Figure 2-13: The electrical impedance measurement of the purchased 25kHz piezo ceramic cylinder in-air and in-water potted in polyurethane.

$$C_0 = \sqrt{\frac{Z_{\omega_r}^2 (\omega_a^2 - \omega_r^2) + \sqrt{(2(\omega_a^2 Z_{\omega_a} Z_{\omega_r})^2 + (Z_{\omega_r})^4 (\omega_a^2 - \omega_r^2)^2)}}{2(\omega_a^2 Z_{\omega_a} Z_{\omega_r})^2}}$$

$$C_m = c_0 \left[\frac{\omega_a^2}{\omega_r} - 1 \right]^2$$

$$R_m = \sqrt{\frac{Z_{\omega_r}^2}{1 - (C_0 \omega_r Z_{\omega_r})^2}}$$

$$L_1 = \frac{1}{C_1 \omega_r^2}$$

When submerged underwater and potted, the potting and water loading on the transducer changes the mechanical behavior of the piezoceramic. There are additional radiation resistance and mass that are added to the system.

For our underwater acoustic modem application, the piezoceramic should be used below but near the resonance frequency so the received response remains flat across its used bandwidth. Therefore, the mechanical resonance frequency is generally above the operating frequency band.

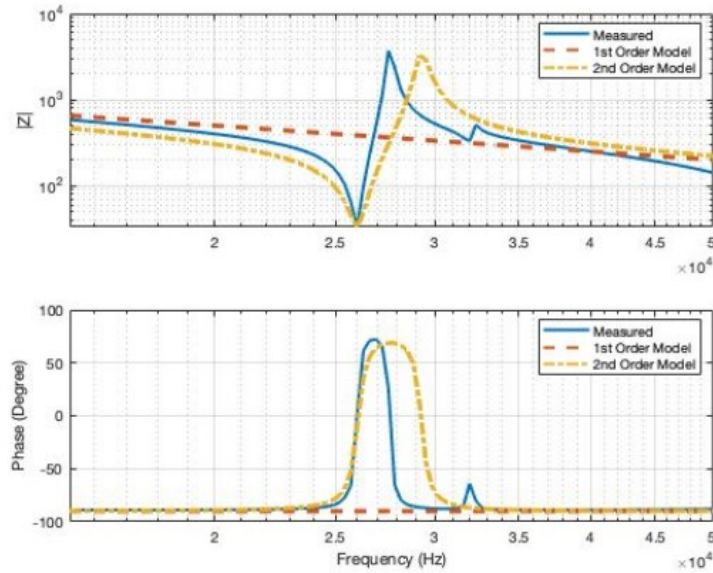


Figure 2-14: Measured and simulated estimated electrical impedance of piezoelectric in air

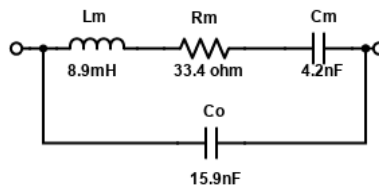


Figure 2-15: Estimated model of the Piezoelectric in air.

2.2.4 Making an underwater Piezoceramic Transducer

Most of the piezoelectric ceramic cylinders will come with outer and the inner surface coated in silver as the conductive surface layer. We need to seal and waterproof the piezoceramic, and make sure it is pressure tolerant in the deep ocean.

First, to prepare the piezoceramic cylinder, we need to solder the wire leads onto the surface. We used 60% tin/40% lead mix solder material. The STEMiNC website recommended 3% silver content solder material to match with the silver coating on the piezoceramic. Since we will be potting the piezoceramic in polyurethane (PU), we selected polyurethane-jacketed cable with 18 AWG 4 conductors for strong adhesion. We applied solder flux on the stripped wire and the target solder spot on the

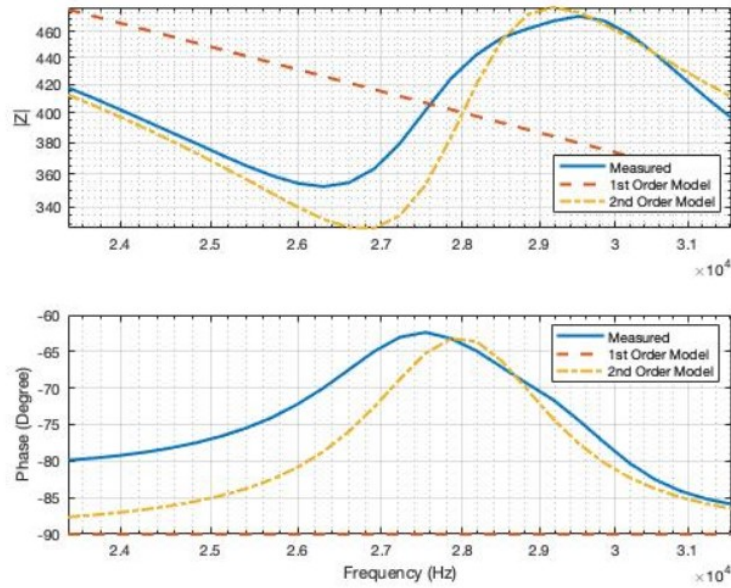


Figure 2-16: Measured and simulated estimated electrical impedance of piezoelectric potted in water

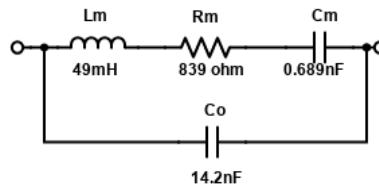


Figure 2-17: Estimated model of the Piezoelectric potted and in-water.

piezoceramic. The piezoceramic's Curie temperature is around 250°C. The soldering temperature should be 250 - 270°C applied for no more than 3 seconds, or else you risk the silver electrode peeling off and cause the piezoceramic to lose its piezoelectric properties. The cable used has 4 wire strands. All four wires are soldered near the center of the piezoceramic cylinder, two wires for the outer electrode, and two wires for the inner electrode. The wires are soldered equally spaced apart, cabling alternating outer and inner electrodes.

Potting is filling an electronic assembly with a solid or gelatinous compound. It is done usually to protect electronics from shock, vibration, moisture, water, and corrosive agents. Common potting compounds are thermoset plastic, silicone rubber gel, and epoxy resins. For our purpose, we will also need the potting material to be

robust and non-compressible. The piezoceramic cylinder is completely encapsulated with the four wire leads coming out. We used a PU potting compound with matching water acoustic impedance for the piezoceramic to make our acoustic transducer. Transmission efficiency is not the only parameter of interest; we also need to be aware of bandwidth and beam shape.

PU potting material is inexpensive and available off-the-shelf. There are a multitude of companies that supply many different types of PU. We are looking for a PU that can help the impedance match between piezoceramic and water. The Smooth-On brand is well-known and one of the easiest to find in stores and online. They offer a variety of different work time, cure time, and hardness for their polyurethane rubber. However, there is no comprehensive testing and evaluation done on the acoustic impedance response of the Smooth-On products. Alfa International Corporation UNWC XP-1 is a PU encapsulation material formulated specifically for acoustical transparency in water. However, it is not readily available off-the-shelf. BJB Enterprises WC-565 is an inexpensive, off-the-shelf, and relatively good impedance-matching material for piezoceramic and water [27].

To pot the piezoceramic, we need to make a mold. The potting material is serving as an acoustic impedance matching layer. Another important factor is the thickness of the matching layer. The thickness of the matching layer should be equal to a quarter of the sound wavelength, to minimize the reflection at the interface between piezoceramic and the potting material [28].

The wavelength is the ratio of phase speed of the acoustic wave over the wave's frequency. The wavelength of 25kHz in PU is approximately 6cm. The recommendation is to have the matching layer approximately a quarter wavelength. The mold is designed to suspend the piezoceramic in the center using the cable leads, allowing the PU to flow around and encapsulate the piezoceramic cylinder. The mold can be 3D printed or constructed using off-the-shelf tubing, plastic sheet, and adhesive.

Potting the piezoceramic requires trial and error. We want to minimize delamination, especially during deployment under high pressure deep in the Ocean. Delamination at pressure is potentially due to the compression mismatch between the two

materials, which results in shear strains at the boundary. Delamination can cause non-obvious electronic shorts, or leaks underwater. Non-obvious because the device may perform well when above a certain depth or during testing, but fail under pressure, or worse, in the field. It is imperative to take great care and caution when potting electronics.

To prepare the mold potting, we first clean, and wipe down the mold with isopropyl alcohol (IPA). The mold is sprayed with the mold release agent, Smooth-On's Universal Mold Release. Following the BJB potting instruction, we applied two coats of Smooth-On mold release, with 10 minutes drying time in between. Then we wipe down any excess mold release using a lint-free wipe. We avoided contaminating the piezoceramic surface with mold release, or else PU potting material will not probably cure and encapsulate the piezoceramic.

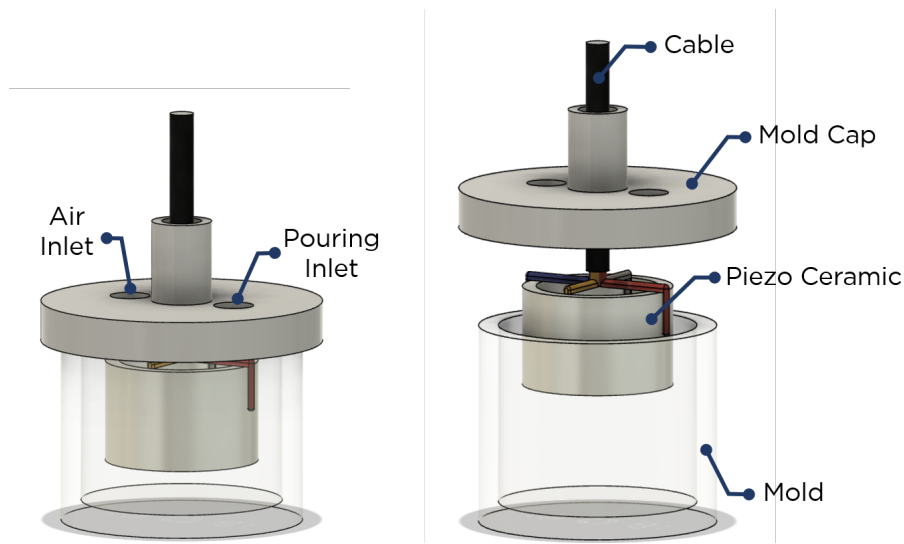


Figure 2-18: Soldered piezoceramic transducer with leads is suspend inside the mold during casting

We prepared the piezoceramic and cable for potting by cleaning and wiping down piezoceramic and cable with IAP using lint-free wipes. We then evenly roughed up the adhesion site of the cable jacket using 100-grits sandpaper. For a better PU potting adhesion to the cable, we applied two even coats of primer to the cable and piezoceramic, with 30 minutes of drying time in between each coat. After drying, we used 100-grits sandpaper to evenly rough up the cable again.

BJB WC-565 has a working time of 15 minutes. The process for potting starts with mixing and degassing the PU resin in a vacuum chamber, then filling the mold with PU, and finally curing under pressure. Degassing and pressure curing eliminate and minimize air bubbles in the PU encapsulation. Air bubbles trapped in the potting will cause scattering.

The BJB WC-565 [29] comes in a two-part resin. Polyurethane is moisture sensitive. The resin will form bubbles in the presence of moisture. Before potting, we left the piezoceramic and the attached cable in a desiccator to remove as much moisture as possible. If possible, we recommend potting in a controlled temperature and humidity location. The BJB WC-565 comes in a two-part mix. The mix ratio of A and B is 1-to-1 by weight. We used a scale to weigh out part A and part B of the PU resin, then combine them together in a mixing cup. We used a non-porous stir stick to avoid introducing moisture, such as a glass stirring rod to mix the resins together. Once thoroughly mixed, placed the combined PU resin in the vacuum chamber and pull as close to a full vacuum as you can to remove any air bubbles. The vacuum pump is powerful enough to pull an appropriate vacuum in about one minute, well within the work-life of the PU mixture. At the low pressure, the bubbles in the mixture will expand and float up. The mixture will start bubbling more vigorously, we made sure to keep a close eye on the mixture so it won't bubble over.

After the bubbling slowed down to 2 to 3 bubbles per seconds, we released the vacuum and poured the degassed PU mixture into the mold with the piezoceramic and cable assemblies. We poured in small streams and steadily filled from the bottom to the top to avoid trapping air bubbles. After the mold is filled, we placed the assembly into a pressure chamber and pressurized to 60psi. The pressurization forced the bubbles back into the PU mixture and shrank any air bubbles that might be still present in the mixture. We let the PU potting cure under pressure for the recommended duration (4 to 6 hours) or overnight. Once cured, we demolded the potted piezoceramic, and we have a potted waterproof and pressure-tolerant acoustic underwater transducer.



Figure 2-19: PU Potted 25kHz piezoceramic transducer with soldered PU jacket 4 conductor cable

2.3 Transmission Board

The piezo transducer works like a speaker underwater. The transmission board takes the signal from the controller board and drives the speaker with the signal at high power. The transmission board is composed of three main components: SEPIC power converter, Class-D power amplifier, and impedance-matching circuit.

The 12-volt battery source is connected to the SEPIC power converter. During operation, the microcontroller adjusts the SEPIC converter power output that feeds into the switching power amplifier. The switching power amplifier is connected to the piezoelectric transducer with the impedance-matching circuit. Transmission is the most power-intensive operation.

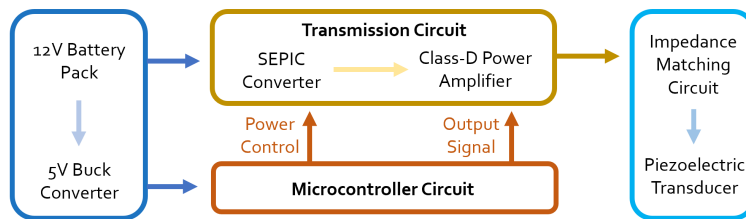


Figure 2-20: Transmission board circuit block diagram

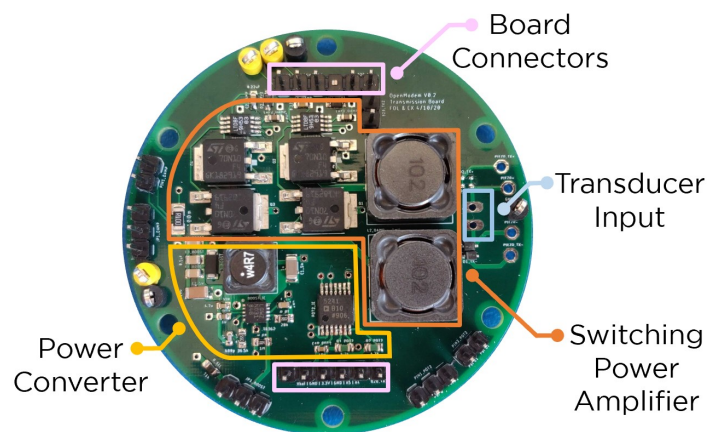


Figure 2-21: OpenModem Transmission Board Version 2

2.3.1 Power Amplifier Design

The transmission signal is generated by the controller board. The controller board signal output voltage is 3.3V and the current is around 7mA. The signal needs to be amplified using a power amplifier. A power amplifier's purpose is exactly as it sounds; it amplifies the input signal's power.

There are many different forms of power amplifiers with trade-offs in cost, efficiency, and linearity. One of the big commercial applications for power amplifiers is for driving speakers, almost the same as our application, except for a few very important key differences. We are driving a piezoelectric ceramic transducer in water instead of a woofer in air. We are driving the transducer at a couple of specific frequencies instead of across a wideband of frequencies. The in-air speaker power amplifier is designed to maintain the linearity of the input signal. Linearity usually comes at the trade-offs of efficiency and cost. We will go over briefly common linear amplifiers and our chosen design, switching amplifiers.

Starting with the simplest and the most linear design, the Class A amplifier. A Class A amplifier uses a single-ended transistor for its output stage with the resistive load directly connect to the collector. The Class A amplifier is constantly biased, therefore there is a continuous loss of power when idle. The efficiency is around 30%, way too low for our application. The Class B amplifier uses two complementary transistors and is configured as a "push-pull" arrangement. A Class B amplifier eliminates the need for DC bias current with improved efficiency around 78%. However, a Class B amplifier has cross-over distortion and are more thermally sensitive. The Class AB amplifier, like the name suggested, is a combination of Class A and Class B amplifiers. A Class AB eliminates the cross-over distortion in Class B by adding a small bias voltage (D1 and D2, biased diodes), resulting in quiescent power loss. Class A, B, and AB are all linear power amplifiers [30]. The low efficiency of the linear amplifiers is ill-suited for our application, we are trading linearity for higher efficiency.

The Class D amplifier, a type of switching amplifier, can achieve an efficiency above 90%. A Class D has a half-bridge MOSFETs configuration, where the output

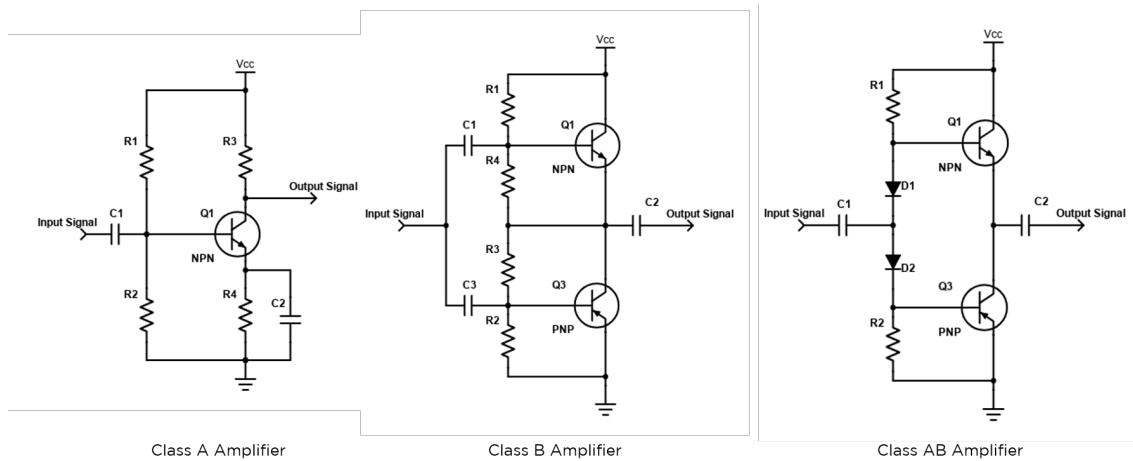


Figure 2-22: Simple version of Class A, B, and AB amplifiers

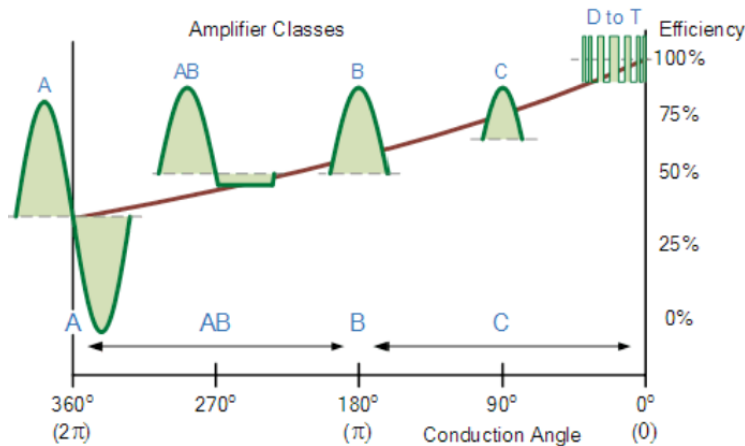


Figure 2-23: Efficiency vs Linearity of different amplifier classes [31]

is switched completely to the positive input voltage or the negative input voltage immediately. The switches are operating at high frequency. The output goes through an LC lowpass filter to filter out unwanted switching noise, then output the desired low frequency. A Class D amplifier can achieve very high efficiency, because the switching MOSFET is either off or in saturation, hence power dissipation comes mainly from switching, which is a small loss. The downside of the amplifier is the non-linearity, which we can mitigate with an impedance-matching filter for the piezo transducer [32]. As mentioned before, the transmission is the most power-intensive operation for the system, efficiency at the power amplifying stage is essential for our application.

For our current design, we implemented a switching amplifier using the H-bridge

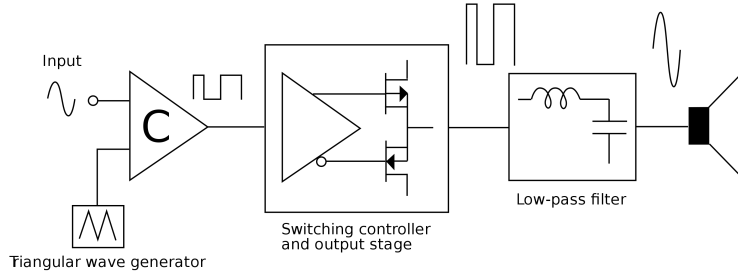


Figure 2-24: Block diagram of a basic switching or PWM (class-D) amplifier

configuration instead of the half-bridge configuration. An H-bridge is 2 half-bridges together. Using an H-Bridge configuration, we can swing from $+V_{input}$ to $-V_{input}$. With higher voltage across the piezoceramic transducer, the louder the transmission. A jumper (JP1) offers the user to selected between direction voltage input from battery or from the SEPIC converter.

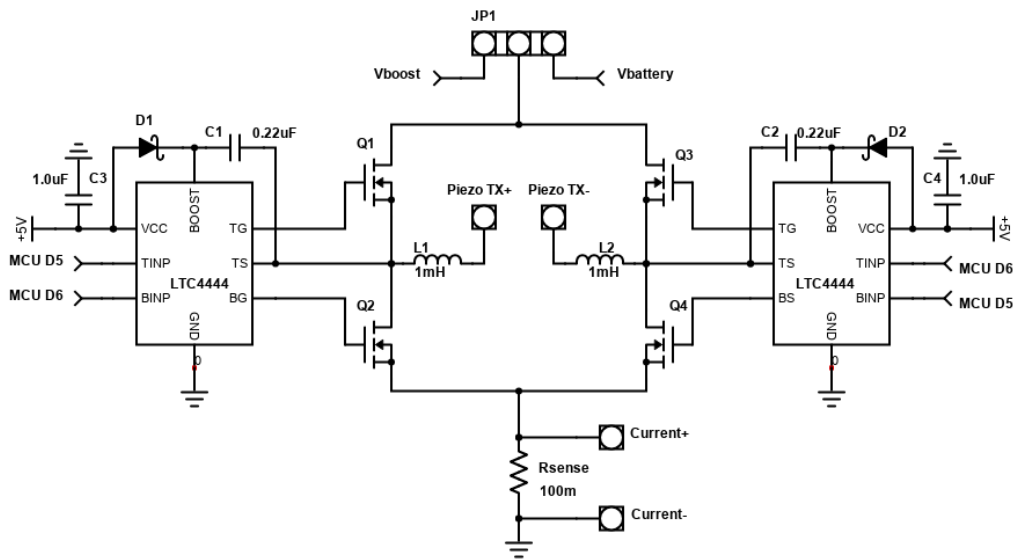


Figure 2-25: Circuit Diagram of the OpenModem switching Power amplifier design

A H-bridge is composed of four switching elements, usually four MOSFET, with the load at the center. The power is connected to the SEPIC power converter. During operation, alternating pairs of MOSFET are turned on and off at the transmission frequency. Therefore alternating voltage is applied across the piezo transducer. The MOSFET is connected by a pair of MOSFET drivers.

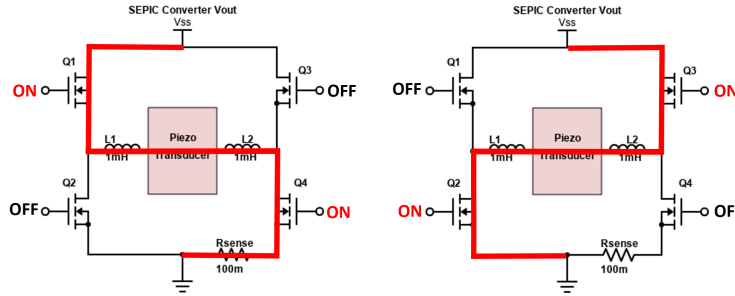


Figure 2-26: Schematic of H-bridge operation, the current direction is reversed when the alternating switches turns on and off

We used 4 N-channel enhancement-type MOSFETs as the switching elements. A N-channel MOSFET, as compared to a P-channel MOSFET, can carry more current, suitable for heavy load.

A MOSFET is a four-terminal device with gate, source, body, and drain. The body is commonly connected to the source. An N-channel MOSFET has n+ region for its drain and source and the body is p-. When a positive gate voltage is applied, a conducting channel is formed between the source and drain. If a voltage is applied between drain and source, the current flows between source and drain. In a H-bridge configuration, the N-channel MOSFETs are used for high-side and low-side switching. High-side is when the switch is between the positive power line and the load. Low-side is switching between the load and the ground. During high-side switching, the voltage at the gate with respect to the ground must be at least $V_{GS} + V_{source}$. To drive the high-side MOSFET, we are using a bootstrap-based MOSFET driver to boost the V_{gate} to above V_{source} .

There are a lot of ICs for driving a pair of high-side and low-side switches, such as IR2110, L6385E, LTC7060. There is also a lot of full-bridge drivers, such as HIP4081A that can driver all four MOSFETs. We chose a pair of LTC4444-5, which can supply bootstrap voltage up to 114V [33]. The gate-source threshold voltage of the On Semiconductor FDD8780, the N-Channel MOSFET of our choice, is 2.5V. Important spec between the MOSFET and the MOSFET driver are the MOSFET's gate capacitance and the MOSFET driver's pull-up and pull-down current. We want to make

sure the MOSFET driver can turn on and turn off the MOSFET above the switching frequency. The gate capacitance of FDD8780, N-Channel MOSFET, in the design is 1 to 1.5 nF [34]. The LTC4444-5 top gate rise time at 1nF load is 8ns, fast enough for our application. The LTC4444-5 also has additional features, such as shoot-through protection to prevent both MOSFETs from conducting simultaneously (shorting the circuit from battery to ground) and under-voltage lockout. The LTC4444-5 takes in two pulse width modulation inputs from the controllers, to drive the high-side and low-side MOSFETs.

A current-sensing resistor is added on the low side of the H-bridge to measure the power and efficiency of the system for evaluation and testing. The resulting proportional voltage across the current sense resistor is amplified using an INA240 instrumentation amplifier evaluation kit with PWM rejection [35]. A subtle consequence is that the resistance in the ground plane is creating a small offset voltage relative to the true ground [36].

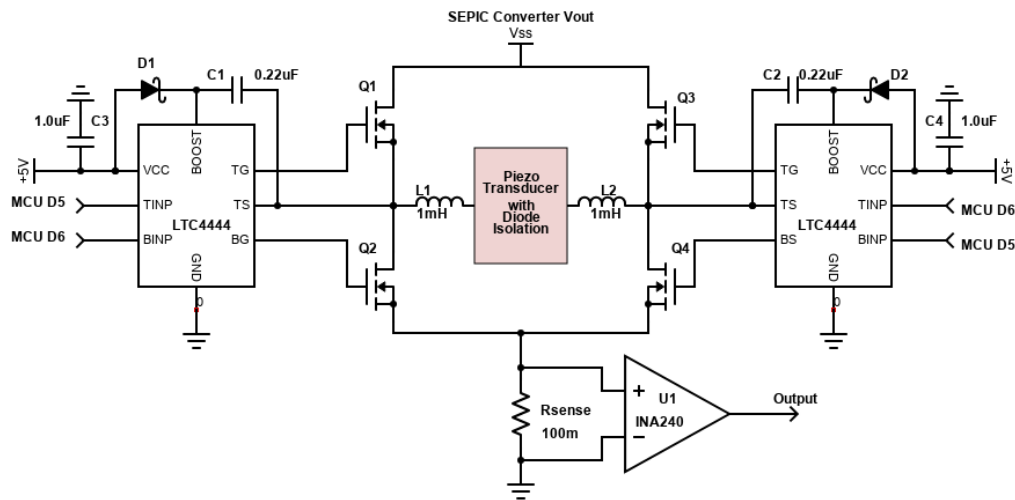


Figure 2-27: Circuit Diagram of the switching Power amplifier with INA240 current amplifier added during testing

2.3.2 Impedance Matching Circuit

Similar to acoustic impedance matching between the piezo transducer to the water, any transmission of power or electric signal requires electrical impedance matching for optimal power transfer. To design the impedance matching circuit, we need to take into consideration the frequency of operation, the impedance of the transmitter, the driver, and the cable. The cable's attenuation increases with cable length and transmission frequency. We are working with a short cable length, 10 cm, at relatively low frequency (<10Mhz). Therefore the cable delay and impedance are negligible. The piezo transducer is the load impedance and the amplifier is the source impedance. Maximum power transfer is achieved from the source to the load if the load impedance is a complex conjugate of the source impedance. Optimizing for maximum power transfer means a better SNR and a more power-efficient design. Impedance matching, as mentioned above, is a compromise between bandwidth and efficiency.

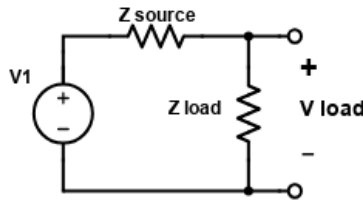


Figure 2-28: Maximum power transfer when Z_{source} matches Z_{load}

The transducer's impedance varies across frequency. Our application will be focused on a narrowband frequency design. Based on the measured and estimated potted Piezoceramic in water RLC model, the piezo transducer is predominantly a capacitive load near its resonant frequency. To matched the electrical impedance of the transducer to the amplifier, we added two 1.0mH inductors in series to cancel out the reactive component of the piezo transducer.

$$f = \frac{1}{(2\pi\sqrt{C_0L_{match}})}$$

The inductor's value was chosen so the circuit from the driver side is mostly

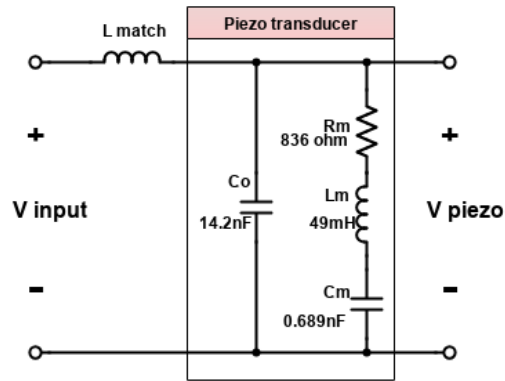


Figure 2-29: Impedance matching circuit with Potted Piezoceramic circuit model

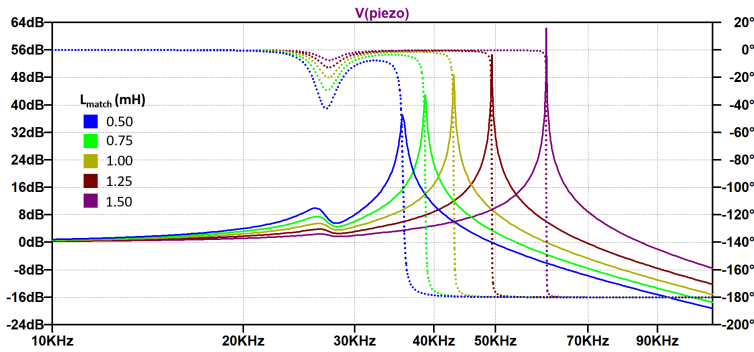


Figure 2-30: Simulated frequency responses with different L_{match} value

resistive (0° phase) around the our frequency of operation, 20kHz to 30kHz. The impedance-matched transmission circuit should be fairly power efficient within this frequency range.

2.3.3 Power Converter Circuit

Directly powering the transducer at 12 volts with the battery pack limits the power output range. Adding a DC/DC converter allows more flexible control over the power output. The modem can operate at higher power in a noisy environment to improve SNR and therefore the transmission rate. It can also operate at lower power in a quiet environment to save energy. There are many different topologies for the DC/DC converter. A DC/DC converter operating principle is to efficiently increase or decrease a supply voltage. In the previous iteration, we employed a boost converter,

producing an output greater than the input. In the current iteration, we employed a single-ended primary-inductor converter (SEPIC). A SEPIC converter is essentially a boost converter followed by an inverted buck-boost converter. It has the advantage of non-inverted output as compare to the buck-boost converter. The SEPIC topology allows the output to be greater than, less than or equal to its input [37]. A SEPIC is essentially a boost converter followed by an inverted buck-boost converter. It has the advantage of producing a non-inverted output as compared to the buck-boost converter.

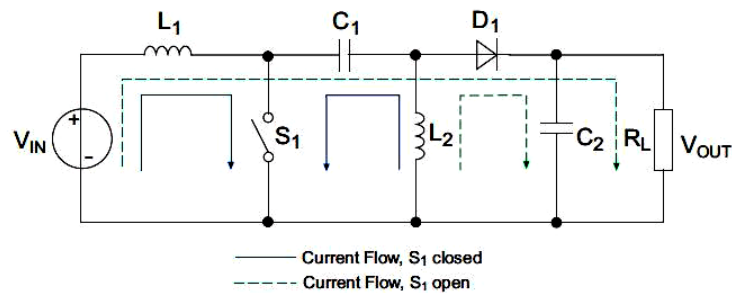


Figure 2-31: schematic of SEPIC converter, with S_1 closed current increase across L_1 and C_1 discharges which increase current in L_2 . With S_2 open, current from L_1 and L_2 goes through the load R_L

There are a lot of DC/DC converters with integrated switch ICs. We used the LT8362 in SEPIC mode. It has a low quiescent current, with a low output ripple. It also has a high switching frequency to minimize interference during transmission. During operation at load currents between 0.2 to 0.3 A, we can reach over 90% efficiency .

The output voltage can be programmed with a resistor divider from the output to the feedback pin. We added a digital potentiometer in place of the feedback resistor to control and adjust the value of the feedback value, therefore, change the output power of the SEPIC converter. A $20K\Omega$ R_T resister sets the switching frequency at 2Mhz based the following formula, where f_{OSC} is the oscillation frequency [38].

$$R_T = \frac{51.2}{f_{osc}} - 5.6$$

The formula for voltage output is shown below. R1 is set at 1MOhm. A higher

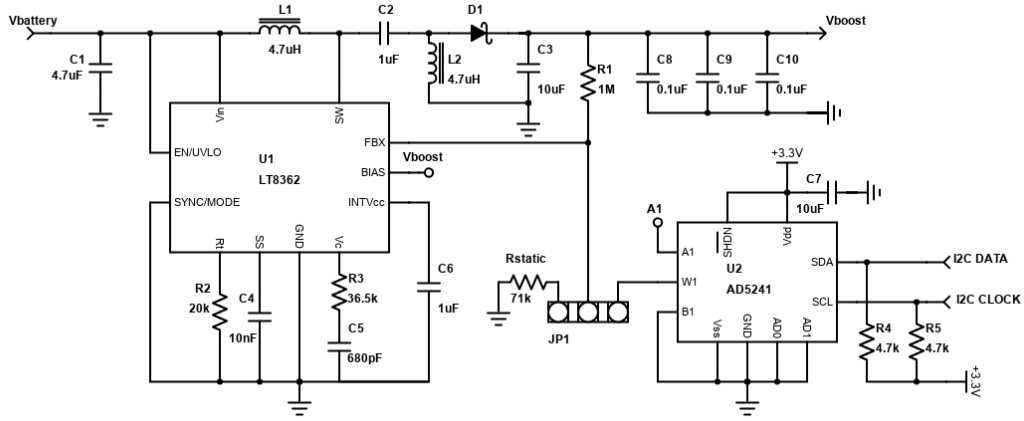


Figure 2-32: OpenModem power converter circuit diagram: LT8362 in SEPIC converter mode with digitally controlled variable output using AD5241 1Mohm digital potentiometer.

value FBX divider resistor results in lower quiescent current draw. By adjusting the AD5241 digital wiper position, we can control the voltage output of the system [39].

$$R1 = R_{AD5241} * \frac{V_{OUT}}{1.60V} - 1$$

$$R_{AD5241} = (1M\Omega + 1) * \frac{1.60V}{V_{OUT}}$$

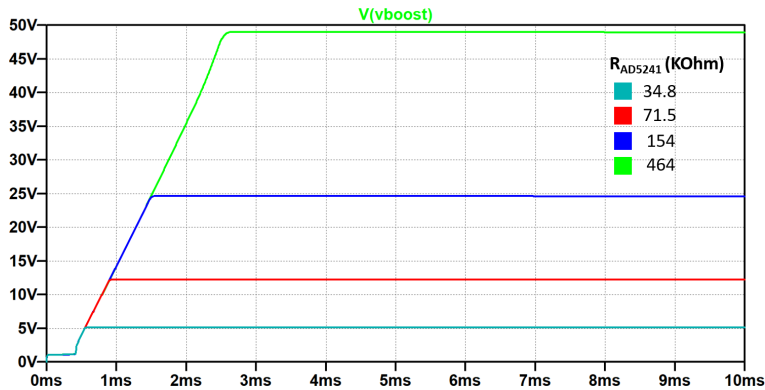


Figure 2-33: Simulation of transient responses and voltage output of SEPIC converter at different feedback resistor values.

2.3.4 Board Connector

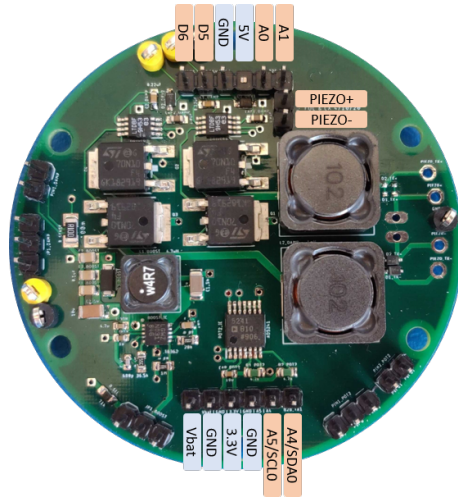


Figure 2-34: Transmission board connector pin out

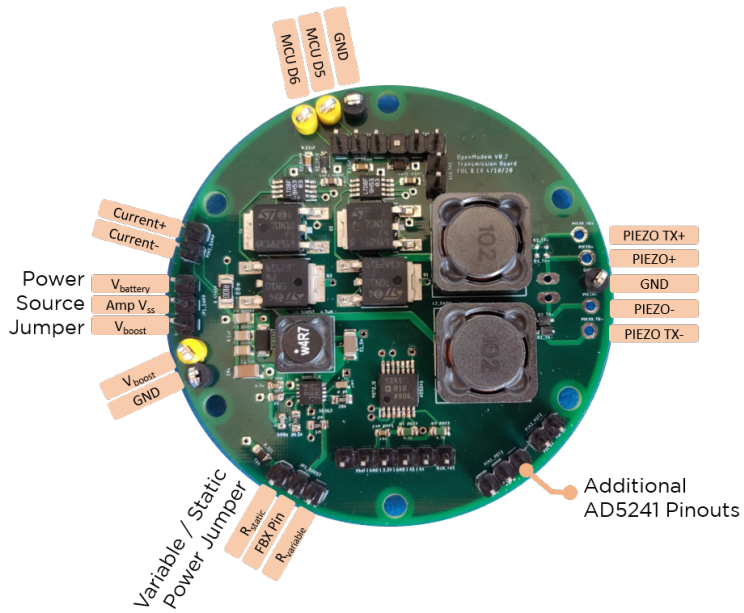


Figure 2-35: Transmission jumper and testing point pin out

2.4 Receiver Board

The piezo transducer also acts as a microphone underwater. The acoustic signal underwater suffers from noise, attenuation, and interference. The receiving circuit buffers the electrical signal generated by the piezo transducer, and outputs a noise-tolerant, low-impedance signal ready for further processing. The RX circuit should amplify the signal around the narrowband operation frequency and filter out higher and lower frequency noise. The RX circuit takes in the signal from the transducers then passes it through an instrumentation amplifier, a bandpass filter, and lastly an autogain controlled amplifier.

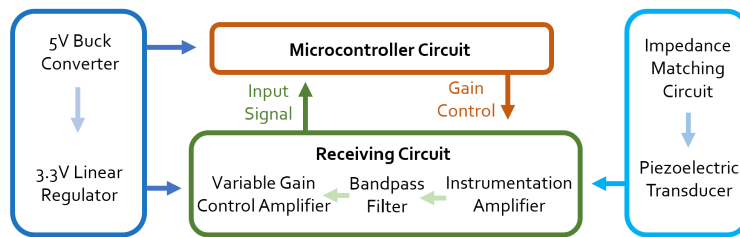


Figure 2-36: Receiver Board circuit block diagram

An instrumentation amplifier (InAmp) buffers the differential signal from the piezo transducer. The output signal is then filtered through the bandpass filter designed at the center operating frequency. Lastly, the filtered signal is amplified again using an autogain control amplifier for an optimal signal amplitude for the microcontroller processing.

2.4.1 Instrumentation Amplifier

The InAmp is a combination of two input buffer amplifiers that feed into a differential amplifier. The advantage of InAmp is that it eliminates the need for impedance matching. The buffer amplifier draws very little current, therefore prevents the piezo-ceramic source impedance from being affected by the load impedance. The differential amplifier eliminates common-mode noise. The purpose of the InAmp in the first stage is to output a low impedance signal with minimal noise for further filtering and amplification.

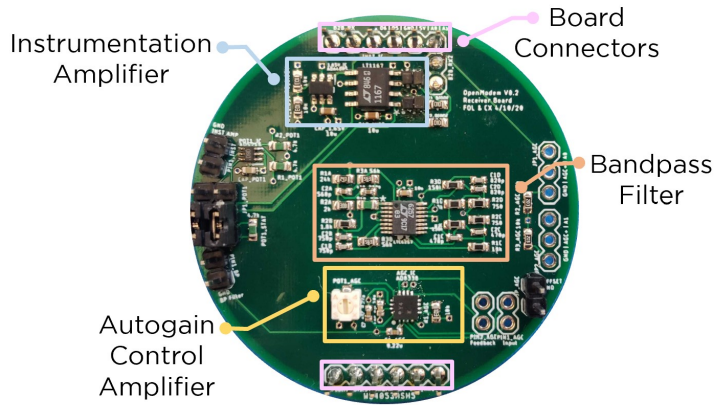


Figure 2-37: Receiver Board

We chose the LT1167 as the monolithic InAmp. The LT1167 is a precision instrumentation amplifier with a high input impedance, good bandwidth up to 1Mhz, high common-mode rejection, and low voltage noise [40]. The gain can be set with a single resistor. In addition, it is a low power amplifier with a maximum current draw at 1.3mA. The maximum voltage input for the microcontroller analog-to-digital converter input is 3.3V therefore, we designed the LT1167 to operate on a single-supply 3.3V.

The key design feature for operating from a single 3.3V supply is to reference the InAmp at the midpoint of the voltage supply. The ADA4805 (U2) is configured as a voltage follower [41]. R1 and R2 form a voltage divider that splits the 3.3V supply voltage in half. The output of U2 provides a low impedance source for the LT1167 (U1) voltage reference. U1 and U2 are supplied with a 3.3V single supply with 10uF bypass capacitors. Since the entire circuit has been level-shifted above ground to 1.65V, the output of the LT1167 must be measured with respect to 1.65V, not 0V.

A voltage divider isn't the most stable voltage reference. It is prone to noise and the effect of fluctuation from the 3.3V supply rail. A shunt reference or Zener diode will provide a more stable 1.65V reference voltage. The benefit of a voltage divider is the flexibility for the system to operate on 5V without switching components or redesign. Another important note is that the LT1167 isn't a rail-to-rail amplifier. The output voltage swings from $-V_s+1.4$ to $+V_s-1.3$. With the 3.3V single-supply

rail, the InAmp output ranges from 1.4 to 2.0 volts. In the later stage, we will further amplify the signal to 3.3V rail-to-rail.

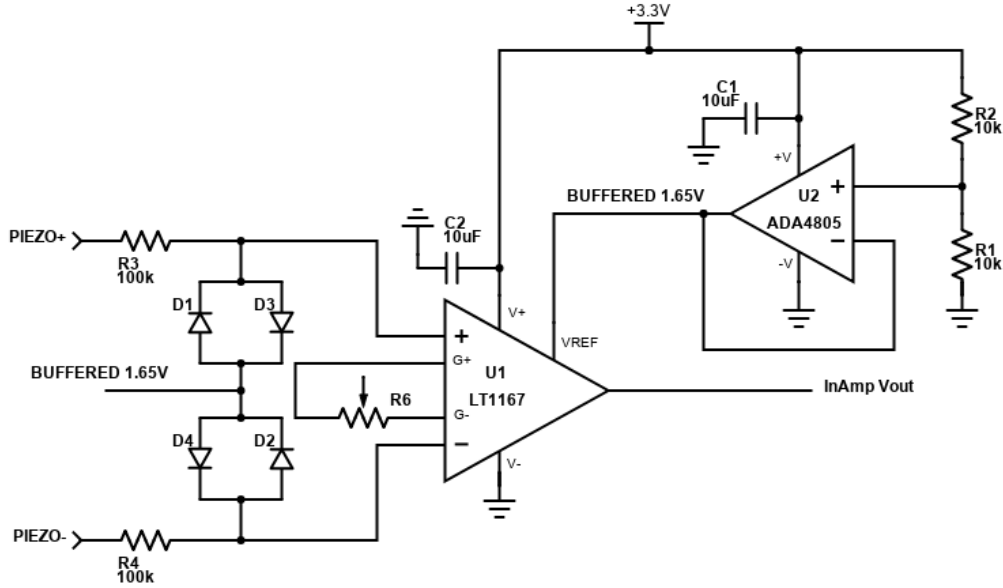


Figure 2-38: OpenModem circuit diagram, Instrumentation amplifier with 3.3V single supply design and 1.65V buffered reference

The piezoceramic transducer is a high impedance, purely differential signal. The high input impedance of the LT1167 (200Gohm) allows the use of high impedance sources without additional offset voltage. We picked the LT1167 due to its high performance and reliability in the trade-off of cost. There is a lot more that can be optimized with the initial stage of amplification. Designers can roll their own instrumentation amplifier or differential amplifiers. There are also lower-cost instrumentation amplifiers such as the AD8608.

During operation, there could be potentially many unknown sources of noise at different levels. In addition, the transmission signal could also vary in power. We implemented a digital resistor, AD5246, to control the gain of the InAmp to prevent oversaturation, and to increase gain for weaker signals [42].

Diode Protection Circuit

The piezoceramic transducer is connected to the transmission circuit and the receiver circuit. During transmission, there are high voltages across the piezo trans-

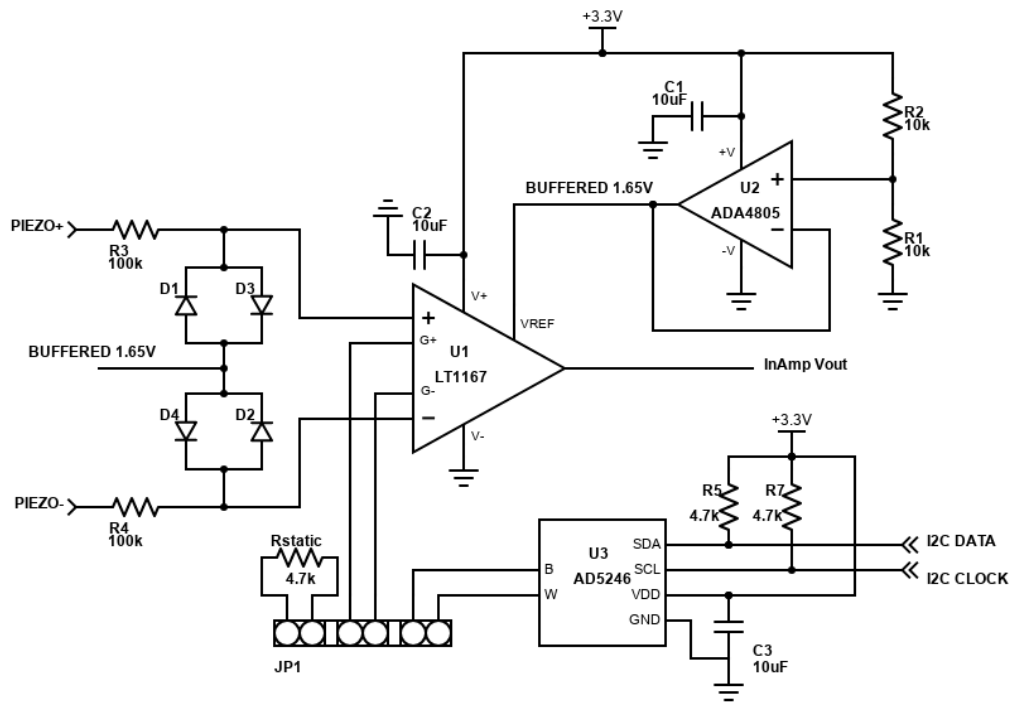


Figure 2-39: Instrumentation amplifier with variable gain control

ducer. The high voltage will destroy the InAmp. Hence, the transmission board voltage output needs to be isolated from the receiver board input.

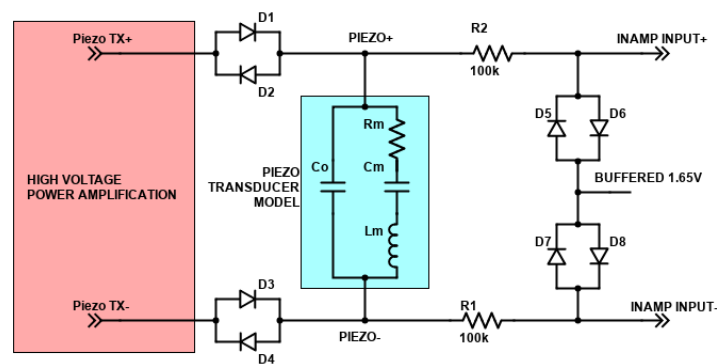


Figure 2-40: Diode protection circuit

A simple protection circuit is implemented using back-to-back diodes to ensure the voltage never exceeds a certain level, protecting the InAmp from high voltage spikes. When the diode (D6) becomes forward biased and is conducting, the piezo transducer input voltage must have input voltage magnitude greater than the buffered reference

voltage by the diode drop. When D6 is conducting, the voltage between InAmp input+ and the reference voltage is clipped at $1.65V + 0.7V = 2.35V$. Thus, with the back-to-back diodes (D5, D6, and D7, D8 configuration), the input voltage across InAmp Input+ and InAmp Input- is limited between 0.95V to 2.35V, and InAmp is protected from over-voltage. The designer can switch out the silicon diodes to Zener diodes, then the input is clipped at the Zener breakdown voltages. Zener diodes are readily available at a wide range of voltage.

However, the LT1167 still has a low input bias current (350pA), therefore a path must be provided for the input bias current. Without the path, the small bias current will produce a voltage across the piezoceramic transducer, and slowly the voltage will drift until the output is saturated. Since the protection diodes are not ideal, there is a small leakage current. The diodes are acting as a very high-value resistor, which provide a discharge path for input bias current.

During power transmission, RX diodes (D5, D6, D7, D8) act as a wire in parallel with the piezo transducer, which will draw all the current away from the piezo transducer. The impedance of the piezo transducer at 25kHz is around $1k\Omega$. Two $100k\Omega$ resistors (R1 and R2) are added to ensure most of the power is delivered to the piezo transducer.

When a signal is received, the piezo transducer will produce a voltage potential. TX diodes (D1, D2, D3 and D4) prevent a current path back to the transmission circuit. The TX diodes selected have a low leakage current and the same forward diode drop as the RX diodes. The power amplifier's output voltage to the Piezo transducer is $V_{tx} - V_{diode} = V_{piezo}$. V_{diode} is the TX diode drop. At higher frequency transmission operation ($>100kHz$), the diode's junction capacitance might affect the drive signal, and cause additional noise and ringing.

In an ideally, noise-free environment, the signal output from the InAmp is purely the acoustic signal received via the piezoceramic transducer. In the real life underwater environment, the signal could include the low humming of a commercial boat or biological noise of close-by marine animals. The key roles of the bandpass filter is for anti-aliasing, and filtering out the noise above the Nyquist frequency of the ADC

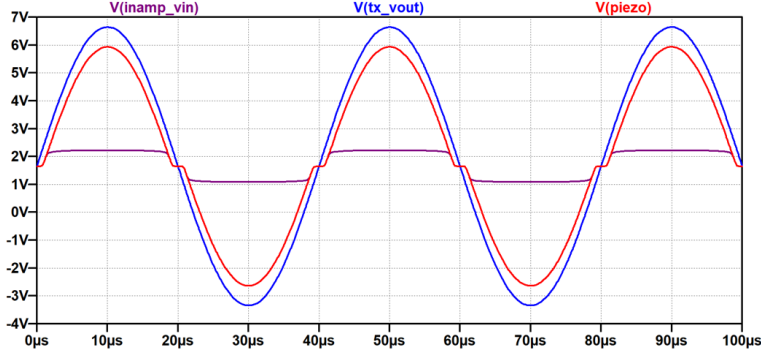


Figure 2-41: Simulation of Diode Isolation circuit with transmission voltage output amplitude, tx_{vout} set at 10V. The diode protection circuit limits the input voltage to the InAmp.

sampling rate. The passband is designed between 15kHz to 30kHz, with a stopband at 50kHz. We implemented a fifth-order Chebyshev filter with four stages.

The bandpass filter is designed using the online filter design by Analog Devices [43]. The bandpass amplifier’s cut-off and center frequencies can be modified by replacing the resistor and capacitor components.

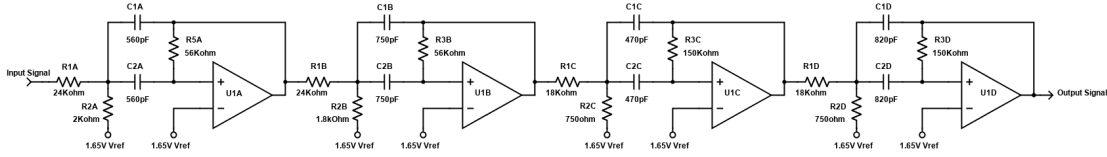


Figure 2-42: Band pass filter circuit diagram

The designer can use a simple low-pass filter around the Nyquist frequency, which is effectively a bandpass filter when combined with the piezoceramic transducers. In combination with oversampling, the process of sampling a signal at a much higher frequency, with the microprocessor, the analog filter cut-off frequency and roll-off can be designed to have less constraints. The digital filter, implemented in processing software, can offer a much harder cutoff. Another capability of a bandpass filter implementation instead of a low-pass filter is undersampling, which allows sampling rate to be lower than the Nyquist rate. Undersampling is a useful technique for higher frequency operation ($>1\text{Mhz}$) with limited sampling rate capability from the microprocessor.

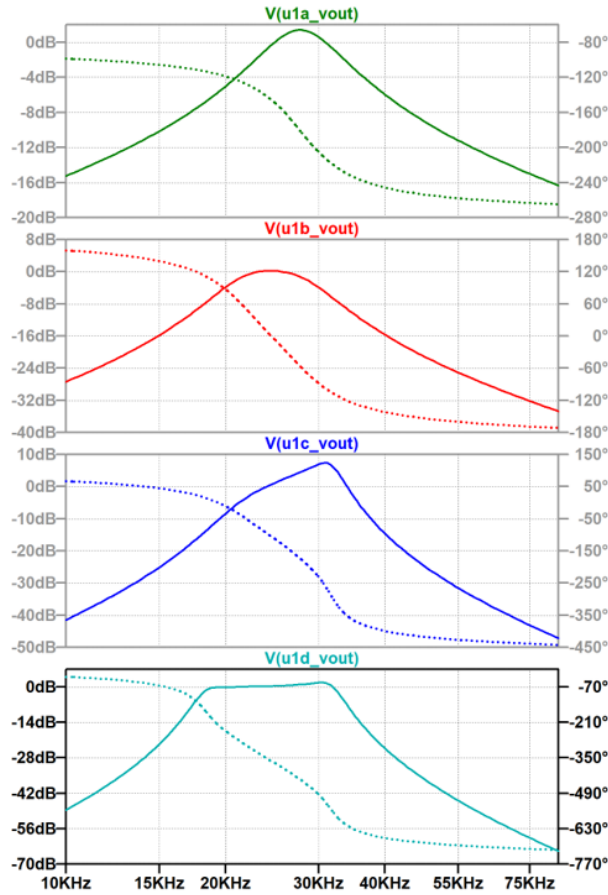


Figure 2-43: Frequency response at each stages of the Bandpass filter

2.4.2 Autogain Control Circuit

The final amplification stage is an autogain control (AGC) amplifier. The purpose of the AGC is to maintain a stable and suitable signal amplitude at its output, despite the variation of the input signal.

We are using the AD8338 Variable Gain Amplifier with an automatic gain control feature [44]. The AD8338 can use a single-supply voltage of 3.0V to 5.0V, and can be very power efficient, needing only 3 mA quiescent current at mid-gain. The automatic gain control block compares the RMS output amplitude of the VGA to the desired RMS output amplitude, then drives the gain to minimize the difference. In steady-state, the circuit forces the RMS output amplitudes to $V_{AGC} - V_{REF}$. The AGC set-point is connected to a manual potentiometer for the user to tune and set during testing. Using the AGC loop, the output voltage is compared against the RMS target

voltage which is defined by the difference between V_{AGC} pin and V_{REF} (1.5V). The AGC uses negative feedback, therefore the MODE pin is set to ground. The AGC attack time is set by C_{AGC} ; without the additional capacitor, the response time is 5us. The AGC recovery time after a transmission burst is within 100us, fast enough for our transmission rate.

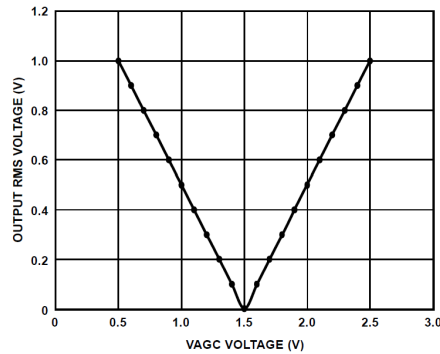


Figure 2-44: Autogain control amplifier V_{AGC} potentiometer control to output RMS output

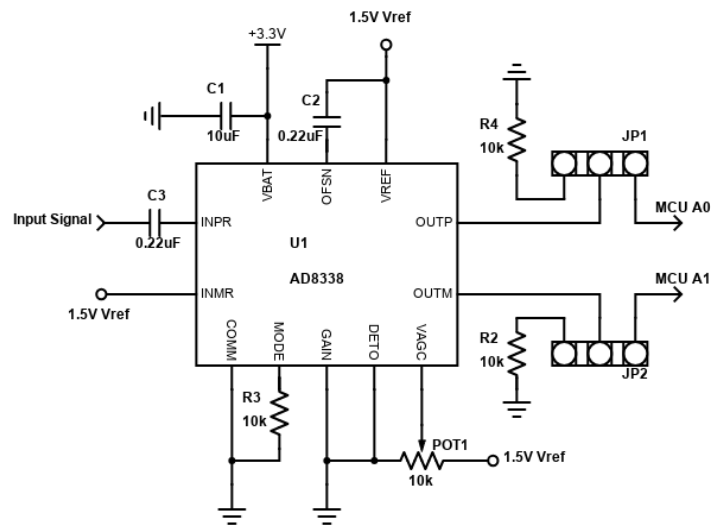


Figure 2-45: Autogain control amplifier circuit diagram

2.4.3 Board Connector

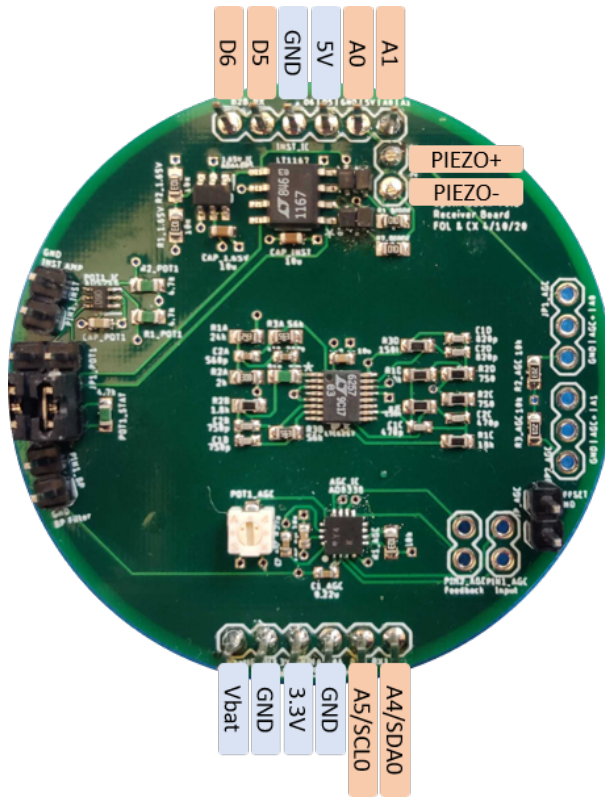


Figure 2-46: Receiver board connector pin out

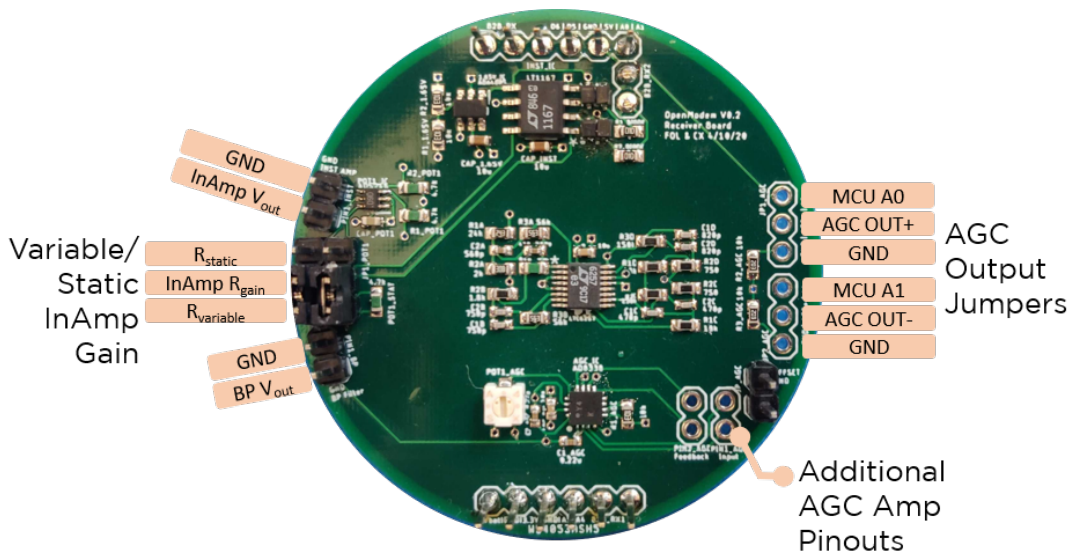


Figure 2-47: Receiver board jumpers and test point pin out

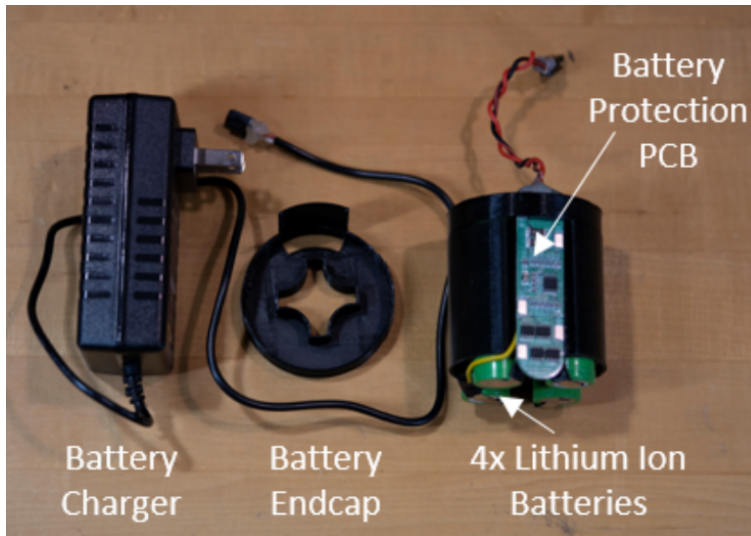


Figure 2-49: 4S battery pack setup

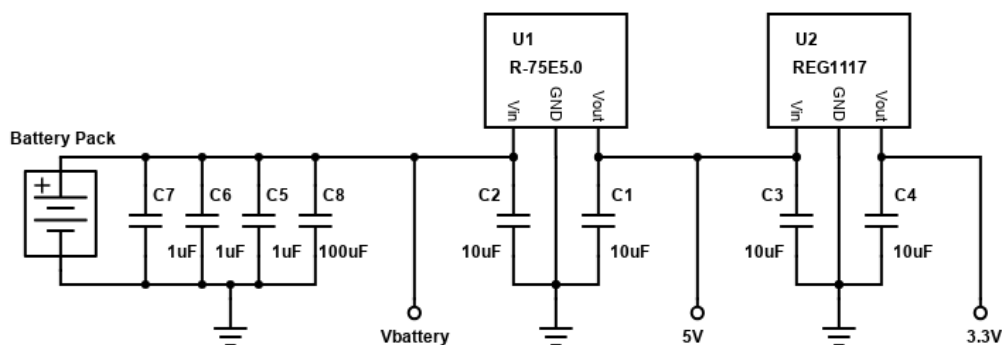


Figure 2-50: Power source management circuit diagram

2.6 Processor Board

The controller we are using in the current design is the Teensy 4.0, which is an inexpensive (\$20), off-the-shelf, and powerful microcontroller supported by a vast tinker community [45]. It can be programmed using the open-source Arduino IDE with Teesyduino Add-On. Teensy 4.0 can either be directly soldered on to the processor PCB or stack-on using headers. Parts of the Teensy 4.0 digital and analog pins are broken out for additional connections.

Teensy 4.0 features the NXP iMXRT1062 chip, an ARM Cortex-M7 at 600 MHz [46]. The most attractive aspects of Teensy 4.0 are its high processing power and

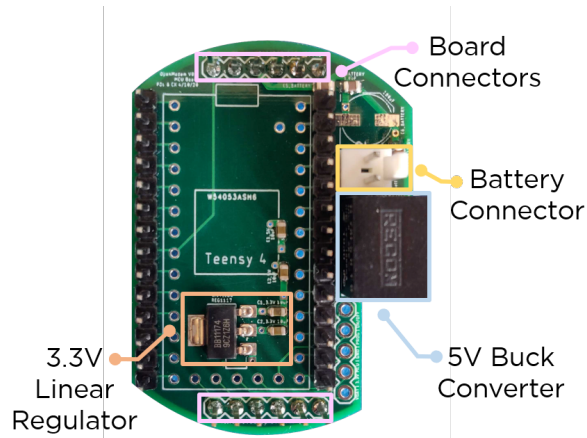


Figure 2-51: OpenModem power management board

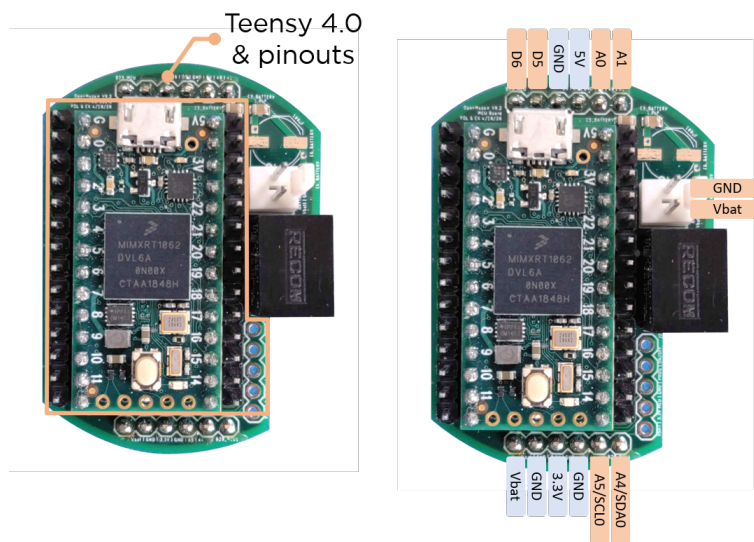


Figure 2-52: OpenModem processor board connector pin out

low cost. The Cortex-M7 core features a Floating-Point Unit (FPU), a very powerful feature when performing digital signal processing. The ADC is a 12-bit successive approximation ADC integrated on-chip. The high processing power enables different software modulation schemes and adaptability for higher-frequency transmission.

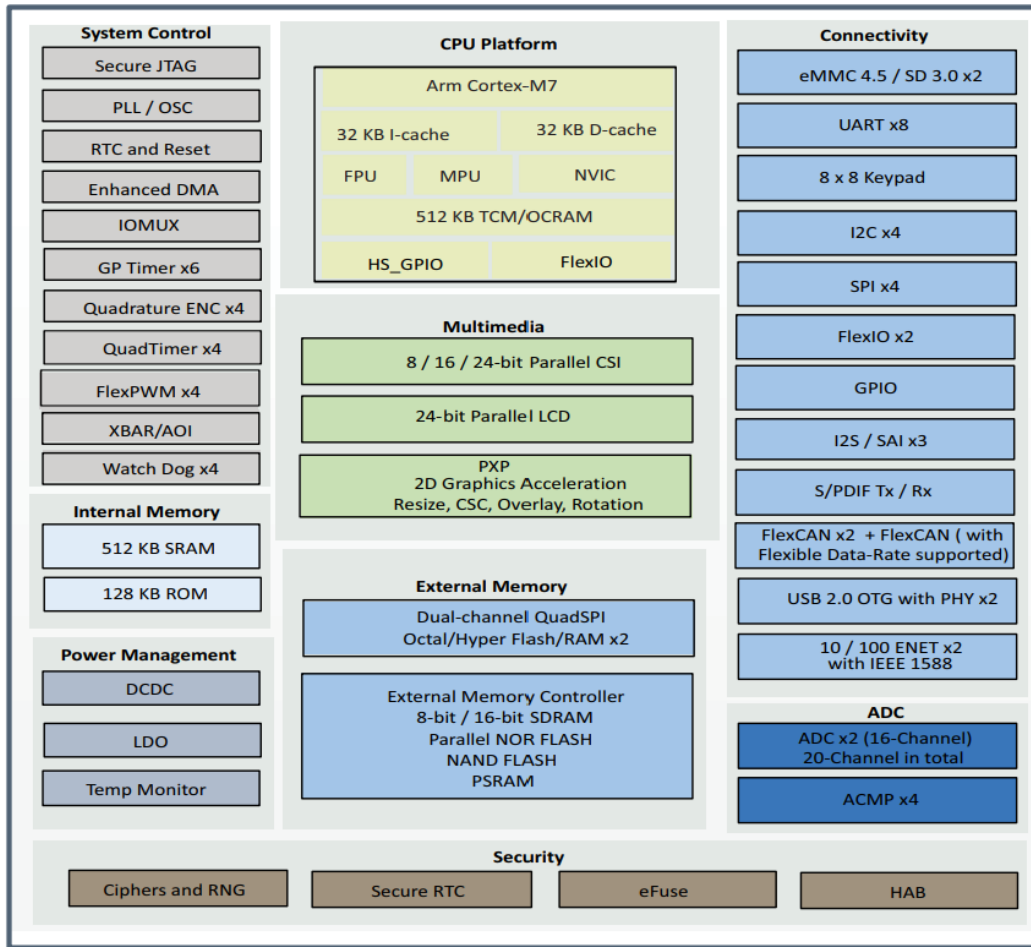


Figure 2-53: Teensy 4.0 iMX RT1060 system block diagram

There are a lot of features available on the chip, but the one that is critical for the modem is the ADC converter block. The conditioned received signal from the receiver board is interfaced with the Teensy 4.0 ADC. We can configure the sample time, conversion speed, and the number of output bits. The starting key parameters of ADC sampling are sample rate and resolution. Its minimal sample rate needs to be twice the Nyquist frequency, at least twice the maximum transmission and receiving frequency. The main advantages of microcontroller over digital signal processors and field programmable gate arrays are design flexibility, adaptability and wide acceptance.

2.7 Housing Design

In order to deploy the modem in the ocean, the mechanics need to be pressure and corrosion tolerant, waterproof, and durable. The three standard options are potting, pressure vessel, and oil pressure compensation system. The potting method encases the device in a compliant potting compound, such as the PU for the piezoceramic. Encasing the electronics in potting component effectively waterproofs the device. Potting requires the potted device to be pressure-tolerant. Components with voids, such as electrolytic capacitors, some fuses, etc. are not pressure-tolerant. Some electronic components are sensitive to pressure changes, which need to be taken into account during the design [47]. In the pressure vessel method, all the electronics are inside a pressure-resistant housing, usually, water sealed with O-rings. The internal electronics are at atmospheric pressure when deployed, isolated from the ocean pressure. The pressure vessel is designed to be reliable and safe up to a certain pressure differential. The oil pressure compensation system eliminates the pressure differential by filling the vessel with electrically insulating oil.

For the current version, we have designed and machined a custom Delrin housing with one O-ring face seal that is pressure tolerant and waterproof down to 1500m. We chose the pressure housing options for adaptability, ease-of-use, and manufacture scalability.



Figure 2-54: OpenModem Pressure Housing

Besides high pressure, the ocean is a corrosive and unpredictable environment. Common housing materials are titanium, titanium alloys, anodized aluminum for

deep deployment. Delrin, acrylic, and PVC are common material for shallow deployment. Traditionally, housing and endcap are machined within in a high tolerance. There are exciting new development of manufacturing pressure housing using additive manufacturing. When designing the housing, the general trade offs are between size, cost, and manufacturability. The OpenModem housing is a thick shell delrin tube and a delrin endcap with O-ring gland.

Pressure (megapascals) increases with depth underwater. h is depth in meters.

$$P = 0.01h$$

For thin-walled vessels, collapse pressure can occur below the elastic limit, which is known as elastic buckling. For tube lengths shorter than L calculated below, collapse pressure can be predicted by the equation below, where r is the tube radius, t is the wall thickness of the tube.

$$L = 4.90r(r/t)^{1/2}$$

For cylinders, elastic buckling collapse pressure, P_e is calculated by the formula below. E is the elastic modulus, μ is the Poisson's ratio, t is the wall thickness, and D_o is the outside diameter of the tube.

$$P_e = \frac{2E}{1 - \mu^2} (t/D_o)^3$$

Inelastic failure for thicker shells occurs at stress levels above the elastic limit. At a pressure value where s_{max} , maximum stress, is equal to yield strength of the material. This is given below, where b is the outer radius of the tube, a is the inner radius of the tube, and p is the external pressure.

$$s_{max} = \frac{2b^2}{b^2 - a^2} p$$

Flat end cap provides support around its edge. The diameter is the unsupported portion of the pate. Failure occurs at the value of pressure where s_{max} is equal to the

material's yield strength, as given below where m is the reciprocal of Poisson's ratio, a is the radius of an unsupported plate, t is the thickness of the unsupported plate, and p is the external pressure, assuming uniform distribution over the plate surface [48].

$$s_{max} = \frac{3(3m + 1)a^2}{8mt^2}p$$

Cylindrical Housing	
Material	Delrin
Outer Radius (cm)	44.45
Inner Radius (cm)	30
Yield Strength (MPa)	55.16
Max Pressure (MPa)	15.01
Max Depth (m)	1501

Endcap	
Material	Delrin
Unsupported Radius (cm)	30
Thickness (cm)	17.7
1/Possion's Ratio	2.86
Yield Strength (MPa)	55.16
Max Pressure (MPa)	15.28
Max Depth (m)	1528

The housing is sealed and waterproofed with a face seal o-ring. The O-ring is made out of an elastomer and designed to be seated in a groove. The endcap and the O-ring groove of the cylindrical housing are designed to hold and compress the O-ring to create a waterproof and pressure-resistant seal at the interface [49].

2.8 Modularity

The OpenModem electronic system is set up to be used as pure transmitter, receiver or both. The transmission and receiver circuits are adaptable up to 2MHz operational frequency for higher data rate and shorter distance communication.

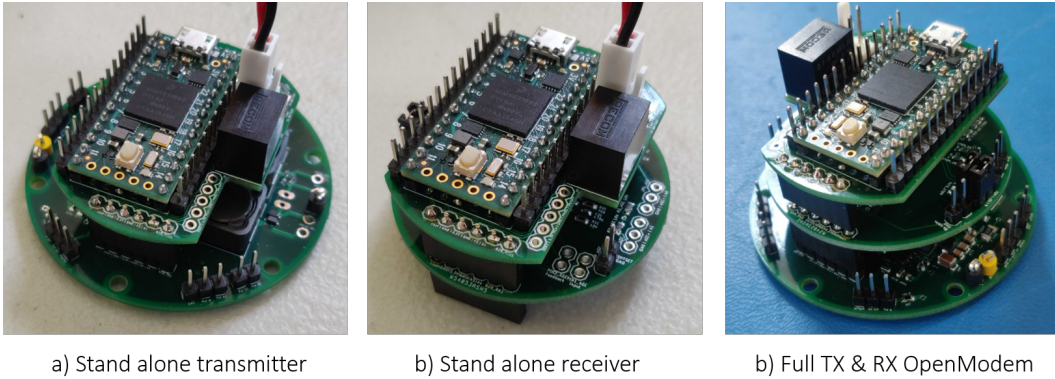


Figure 2-55: Modular OpenModem Setup

Chapter 3

Digital Design

3.1 Overview

We are evaluating a variety of modulation and demodulation routines. On-off keying and frequency-shift keying modulation schemes are based on energy detection, which does not require carrier-phase tracking. The main advantages of these modulations are reliability and simplicity, at the tradeoff of low spectral efficiency. Coherent modulation, with the additional barrier of multipath, requires more complex computations. Phase-shift keying and quadrature amplitude modulation are more spectrum efficient but are more complex, plus require adaptive feedback to mitigate Doppler effect and multipath. Effective bandwidth utilization can be improved by efficient multipath and Doppler correction algorithms and efficient error correction mechanisms. As this acoustic modem has limited battery power, energy efficiency at the physical layer is mandatory. High computation power has a tradeoff between cost and power consumption.

With the hardware setup and ready to go, we need to encode the data for communication. On the physical layer, we covert some information, data or commands, into bits, 0s, and 1s. Channel encoding converts the binary bits into a modulated acoustic wave that travels across the physical channel. On the receiving side, the system decodes the acoustic signal back to the information, data, or commands. By choosing different modulation and demodulation schemes, we can optimize for the

maximum number of bits per joule and the number of bits per unit of cost.

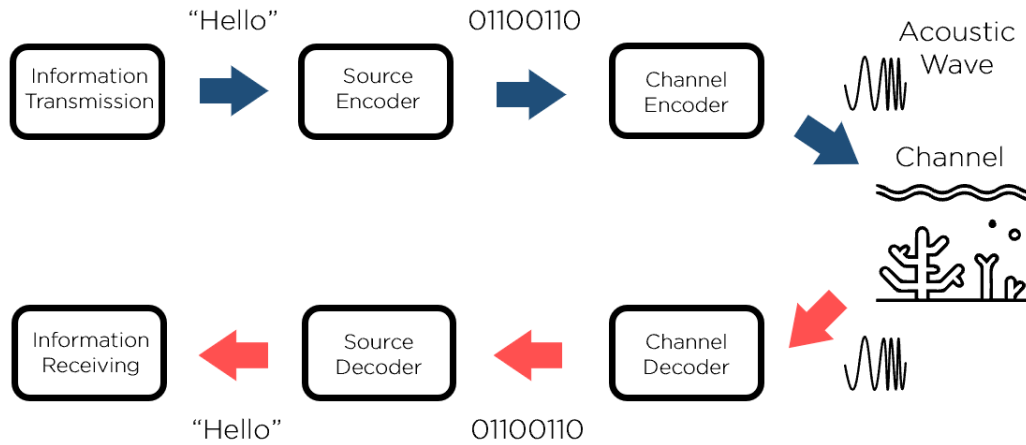


Figure 3-1: Simplified diagram of digital underwater acoustic communication physical layer

3.2 Frequency Modulation

One of the simplest modulation schemes is On-Off keying, (OOK). When the carrier signal is over a certain threshold, the data is high and when the carrier signal is below or absent, the data is low. OOK is sensitive to noise, especially detrimental in an unknown environment. Frequency modulation is more resistant to noise. Frequency-shift keying (FSK) is when the digital information is transmitted through discrete frequency changes of a carrier frequency. The simplest FSK is binary FSK (BFSK), where two discrete frequencies are used to transmit binary data, 0s, and 1s [50]. BFSK encoding and decoding is relatively simple to implement.

3.2.1 BFSK Encoding

The mechanical resonant frequency of the piezo transducer is around 25kHz. We want to work close to the mechanical resonant frequency for a high Q factor, high power efficiency, and output. We selected 24kHz and 28kHz to encode 0s and 1s for testing. When the modem is transmitting 1s, encoded at 28kHz, teensy’s periodic interrupt

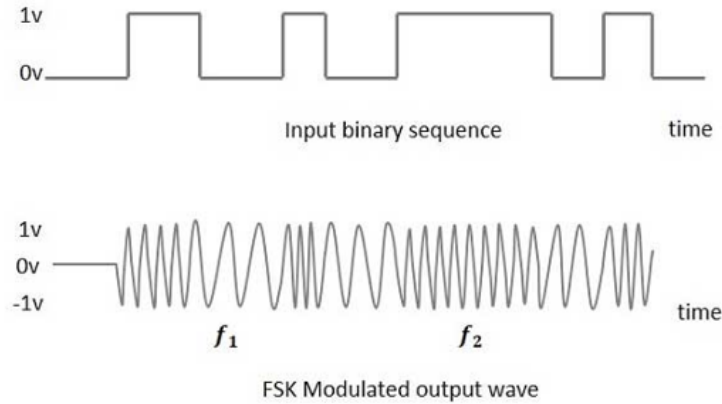


Figure 3-2: Diagram of Frequency Shift modulation encoding

timer (PIT) turns on and generates an interrupt at twice the encoded frequency, 56kHz for the calculated number of counts. During the interrupt routine, two digital output pins are flipped to either high or low states, generating the square wave input signal to the transmission board.

3.2.2 BFSK Decoding

To decode the received signal, we need to accurately identify the presence of a 24kHz or 28kHz signal. There are two major demodulation methods, FM detector demodulators, and filter-type demodulators. [2] We implemented a digital matched filter detector using the Goertzel algorithm.

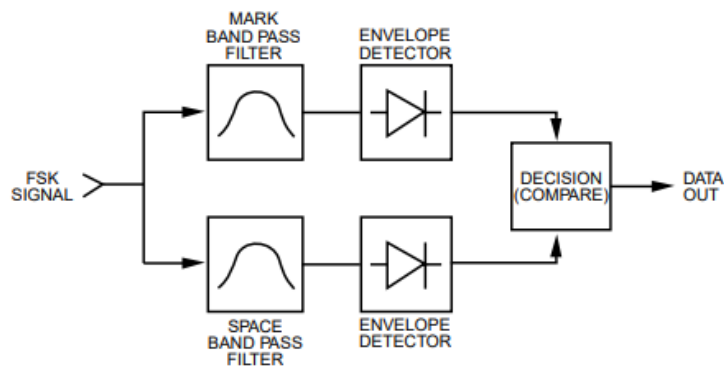


Figure 3-3: Block diagram of matched filter FSK demodulator

The Goertzel algorithm is an efficient method of calculating the discrete Fourier transform for a small number of frequencies, even faster than the fast Fourier transform [51]. The Goertzel algorithm implements the DFT as a convolution of an N-point input, with the impulse response.

$$H_k(z) = \frac{(1 - W_N^k z^{-1})e^{-j2\pi k}}{1 - 2\cos(2\pi k/N)z^{-1} + z^{-2}}$$

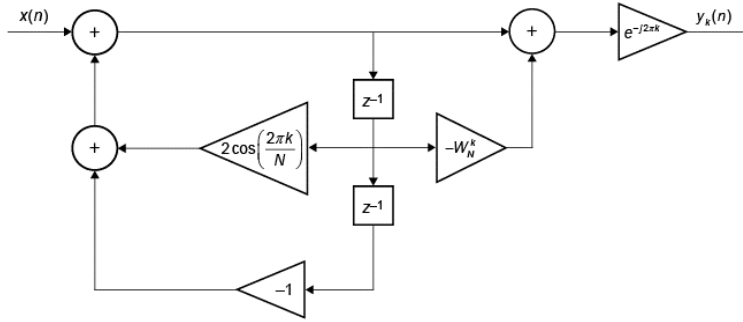


Figure 3-4: Direct form II implementation of Goertzel Algorithm

The basic Goertzel process returns the real and imaginary frequency components. To use the Goertzel algorithm, we first decided on the sampling rate and the sample block size, then we precomputed the coefficient. The sample rate is set at 100kHz, way above the Nyquist frequency. The sample block size is set at 100. The sample block size, similarly in the FFT, controls the frequency resolution. If the sampling rate is 100kHz, the sample block size, N, is 100 samples. Then the frequency bin width is 100kHz/100 = 1kHz. The larger the bin size, the higher the frequency resolution, the longer the sampling time. In the current version, the coefficient is hard-coded in the program.

As a starting condition, we set the index value number, calculate the sin and cos coefficients based on the sample and target frequency, and set the initial value to 0.

$$k = (\text{int})(0.5 + \frac{Nf_{\text{target}}}{f_{\text{sample}}})$$

$$\omega = \frac{2\pi}{N}k$$

$$s[-2] = s[-1] = 0$$

For every sample, we update the calculated value.

$$s[n] = 2\cos(\omega)s[n-1] - s[n-2] + x[n]$$

$$s[n-2] = s[n-1]$$

$$s[n-1] = s[n]$$

After running the loop for N times, we can evaluate the DFT term.

$$real = s[N-1] - s[N-2]\cos(\omega)$$

$$imaginary = s[N-2]\sin(\omega)$$

$$magnitude^2 = real^2 + imaginary^2$$

$$magnitude^2 = s[N-1]^2 + s[N-2]^2 - s[N-1]s[N-2]2\cos(\omega)$$

Lastly, we implemented a threshold detector and a decision slicer based on the agreement upon bit rate. Performance of the implemented decoding algorithm is simulated in MATLAB. Simulated multipath and random noise are included and tested in the simulation. The sample rate is set at 100Mhz. The 0 bit is encoded as 24kHz and 1 bit as 28kHz.

To test the signal to noise to error rate performance of the decoding algorithm, 1000 random bit are generated and encoded with noised added. The decoding algorithm can successfully decode the transmitted signal up to 10 dB in SNR.

With the implemented BFSK encoding and decoding schema, the maximum stable bit rate is 2000 bits per seconds. However in the ocean, depending on the location there could be severe multipath and Doppler spread, so to combat intersymbol interference, wait intervals are added in between bit transmissions for channel clearing. As a result, the in field performance of the FSK scheme is lower than simulated.

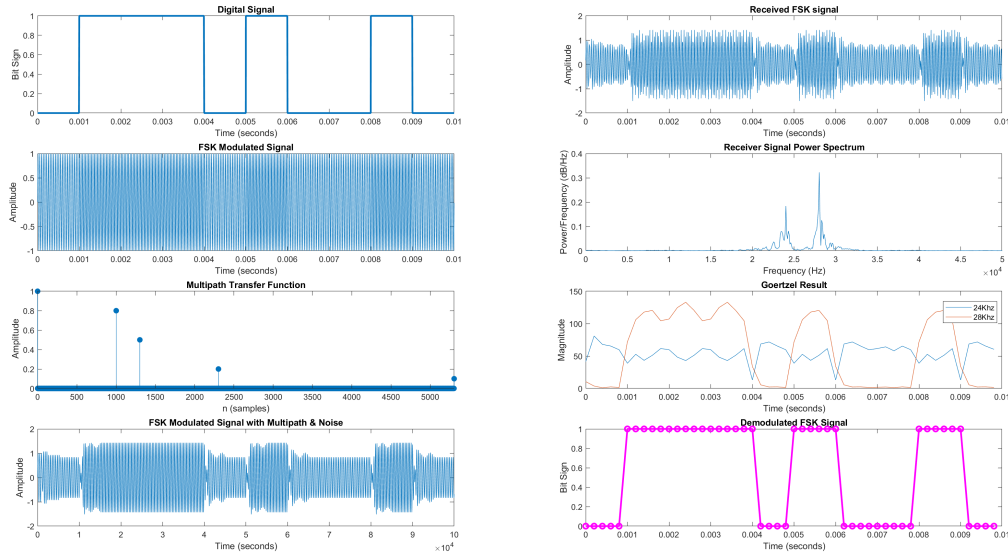


Figure 3-5: Simulation of FSK decoding algorithm, bit rate is set at 1000 bits per second. A 10 bit signal (0 1 1 1 0 1 0 0 1 0) with multipath and noised added is encoded and successfully decoded.

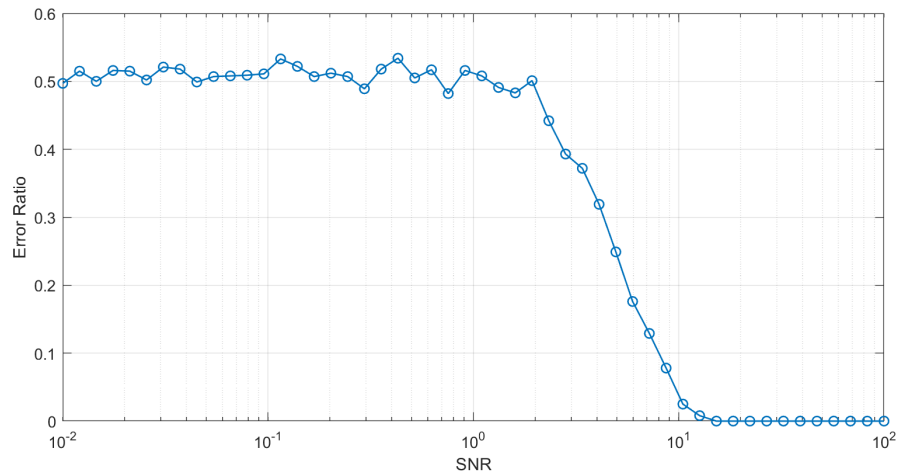


Figure 3-6: Bit error ratio performance of the BFSK decoding algorithm at different signal to noise ratio, at 200Hz bit rate.

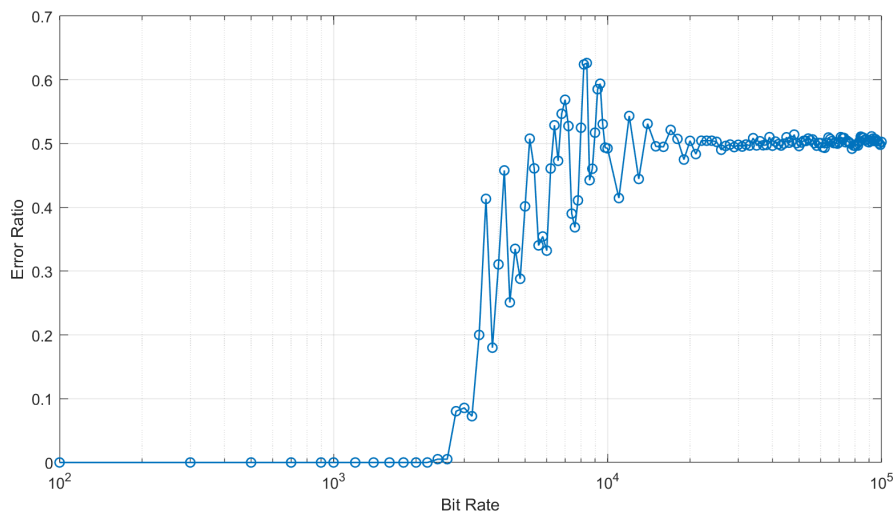


Figure 3-7: Bit error ratio performance of the BFSK decoding algorithm at different bit rate

3.3 Phase Modulation

Another modulation method besides amplitude and frequency is phase shift keying (PSK). Binary phase-shift keying (BPSK) is when the 0s and 1s are encoded with two different phase states in the carrier signal, both phase-separated by 180° . For quadrature PSK (QPSK), each phase is separated by 90° . We can also increase the phase-separation by M for M-ary PSK. PSK offers a better bit error rate than frequency modulation. To demodulate a PSK signal, we need to compare the received signal phase with a reference signal phase to determine the phase shift. The transmitter and the receiver need to be synchronized. However, in the ocean, a variable and constantly changing acoustic channel, the amplitude, and phase of the signal may vary over time. We implemented differential binary phase-shift keying (DBPSK) to eliminate the need for a phase reference between the transmitter and receiver. DPSK can be demodulated using an incoherent demodulation scheme, and has a higher error rate than PSK, since the next symbol depends on the previous symbol's decoding [52].

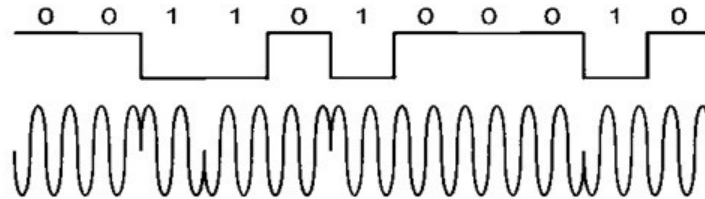


Figure 3-8: Diagram of differential binary phase Shift modulation encoding

3.3.1 DBPSK Encoding

The carrier frequency is set at 24kHz, near the mechanical resonance, 25kHz, of the system for high power output. To implement a phase shift transmission using a switching power amplifier, we added a delay signal transmission. For a 180° phase shift, we added a half period of delay in the signal.

Similar to the FSK modulation code, we are using an interrupt timer on the

Teensy 4.0 to control the timing of the signal. The interrupt timer is set to trigger at every 48kHz, twice the carrier frequency, to toggle the transmission pins. When implementing a 180° phase shift, the toggle is stopped for two toggle counts. For higher M-ary PSK, the interrupt timer can be reloaded with the right timed delay in the transmission signal.

3.3.2 DBPSK Decoding

To decode the DPSK signal, we are comparing the previous bit phase to the current bit phase. If there is a 180° phase shift, then the current bit is 1. If there is no change in phase, then the current bit is 0. The Goertzel algorithm that we implemented for FSK demodulation can be used to calculate the phase shift for PSK demodulation.

$$phase = atan\left(\frac{imagary}{real}\right)$$

The performance of the implemented DBPSK decoding algorithm is simulated in MATLAB. The sample rate is set at 100Mhz. The 0 bit is encoded as no phase shift, and the 1 bit is encoded as 180° phase shift. The DBPSK bit error ratio to SNR performance is better than for BFSK, and the DBPSK bit error ratio to bit rate performance is similar to the BFSK performance. The limit on bit rate is set by the carrier frequency. At a higher carrier frequency we can achieve higher bit rate. By using a higher mechanical resonant frequency piezo ceramic transducer, we can increase the carrier frequency.

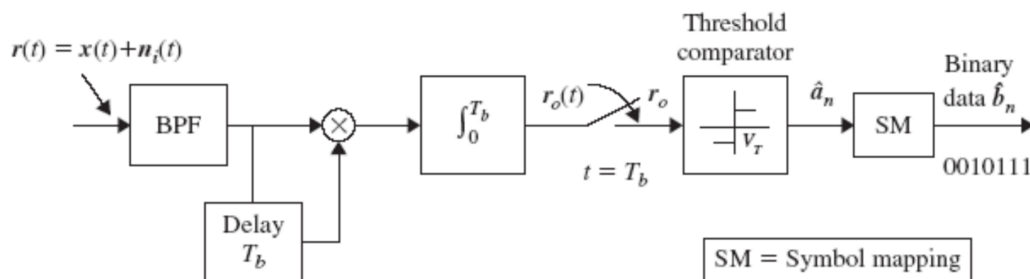


Figure 3-9: Block diagram of non-coherent DBPSK decoder

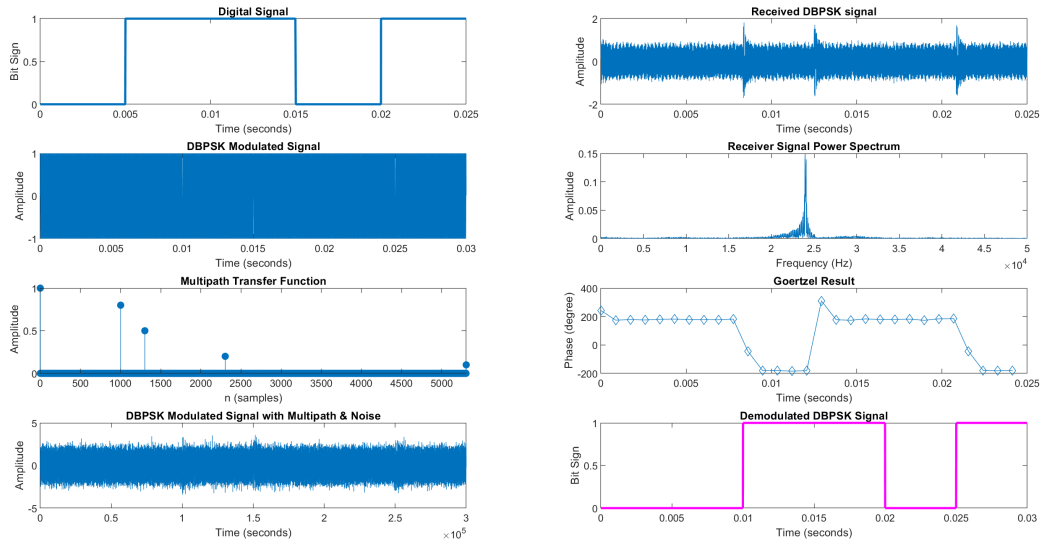


Figure 3-10: Simulation of DBPSK decoding algorithm, bit rate is set at 200 bits per second. A 5 bit signal (0 1 1 0 1) with multipath and noised added is encoded and successfully decoded.

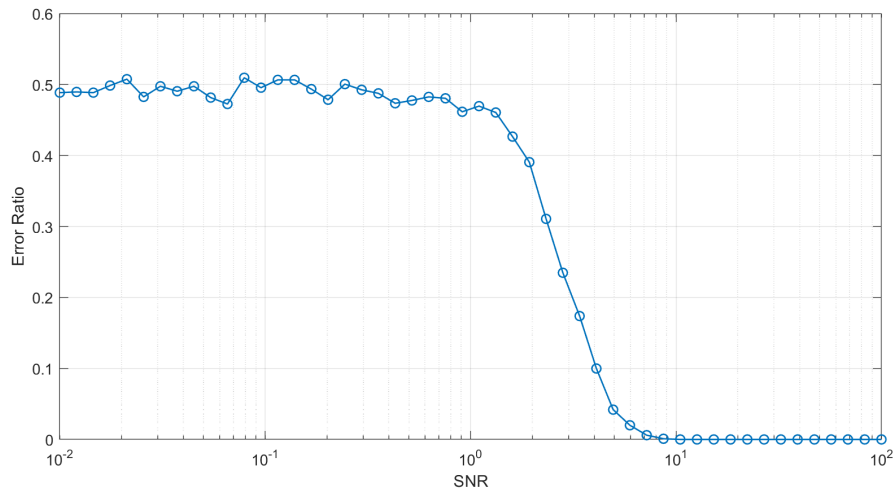


Figure 3-11: Bit error ratio performance of the DBPSK decoding algorithm at different signal to noise ratio, at 200Hz bit rate.

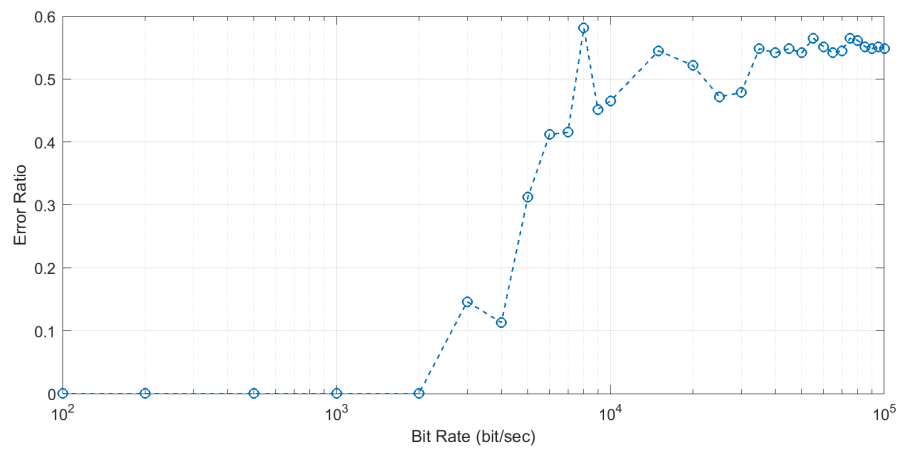


Figure 3-12: Bit error ratio performance of the DBPSK decoding algorithm at different bit rate

Chapter 4

System Test and Evaluation

4.1 Overview

To evaluate the operation of OpenModem, we tested the transmission and receiving performance with BFSK and DBPSK modulations implementation. We performed preliminary testing in a small contained environment. We measured the bit error rate performance of both modulation schemes, and transmission and receiver power consumption during operation.

4.2 Water Tank Test

For our initial in-water tests, we set up the testing environment in a 67cm by 35cm by 37cm tank. The transmission modem transducer is placed 50cm away from the receiver modem transducer. The modems are powered by a benchtop variable power supply at 12V. During testing, both transducers are submerged and suspend in water. Due to the small size of the testing container and the hard reflective water-to-air boundary and water-to-wall boundary, we expect a shorter multipath spread, longer ringing, and settle time than an open environment. Also, the water tank has its normal vibration modes that are excited during transmission. Due to the size and material constrain of the water tank test, we are unable to evaluate the power output and transmission distance. The water tank environment is a distinctly different en-

vironment than in the field, an open water environment. The water tank test serves as a preliminary verification of the modem's performance. The performance of the modem should be tested in the deployment environment before official deployment.



Figure 4-1: The water tank test set up

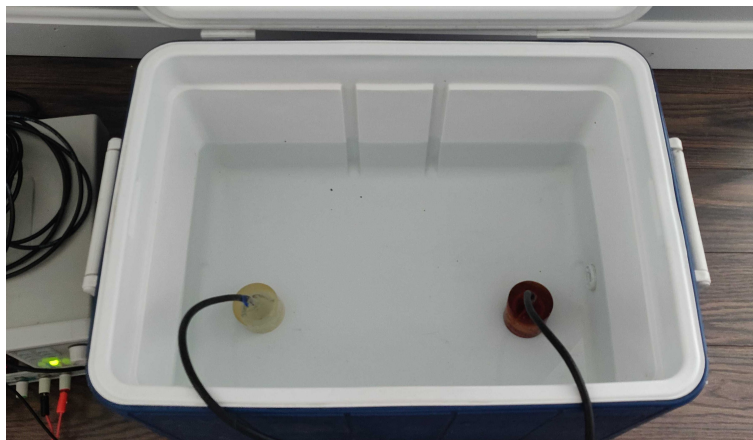


Figure 4-2: Positions of receiver and transmitter piezo transducers in the water tank

4.2.1 BFSK

For the initial BFSK modulation in-water test, we measured the analog voltage across the transducer during transmission and receiving. The analog signal of a 4-bits [0 1 1 0] signal was transmitted and received. The 0 bit is set at 24kHz and the 1 bit is set at 28kHz. The bit period is set at 5ms, with a 5ms wait interval for the ringing to attenuate. The receiver board amplified the piezo transducer signal. From

the receiver signal, we can see the ringing and normal mode vibration after each bit during the waiting interval. The power spectrum of the receiver signal shows two distinctive peaks at 24kHz and 28kHz.

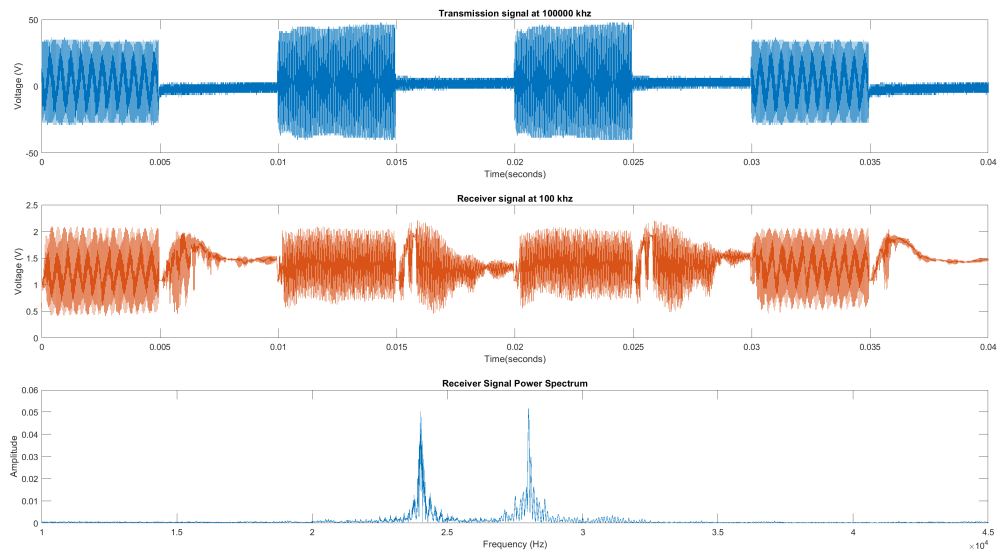


Figure 4-3: BFSK modulated analog signals of transmission and receiving modem

To verify the operation of BFSK digital decoding, we sent a package of 100 bits. The package is transmitted at 100hz bit rate, 5ms bit duration with a 5ms waiting interval. The receiver modem was able to successfully demodulate the transmitted package.

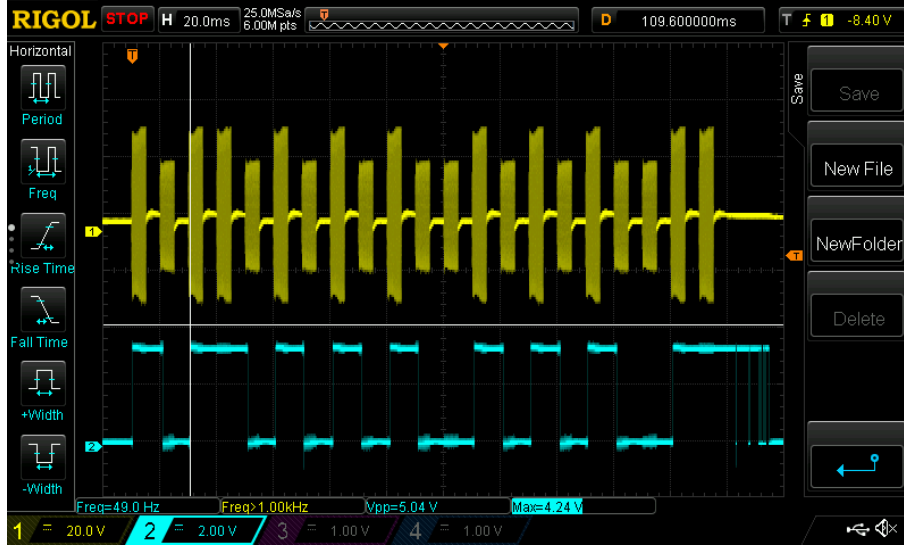


Figure 4-4: The yellow trace is the transmission signal at 100 bits per second. The blue trace is the decoding BFSK output

The 386 μ s delay between the transmission signal and the receiver digital output is due to the acoustic sound delay and initial demodulation integration time. The speed of sound underwater is 1500 m/s . The distance between the transmitter and receiver is 0.5m. It took 333.3 μ s for the signal to travel. The initial receiver demodulation integration took 40 samples, at 100kHz sampling frequency is equal to 40 μ s. Using the BFSK modulation scheme, the delay can be estimated based on the formula below, D is the transmission distance in meter, v is the speed of sound in water and N is the bin size of the Goertzel Algorithm, and f_{sample} is the processor sampling frequency. The estimated delay for BFSK transmission in the test tank is 373.3 μ s.

$$delay_{BFSK} = \frac{D}{v} + \frac{N}{f_{sample}}$$

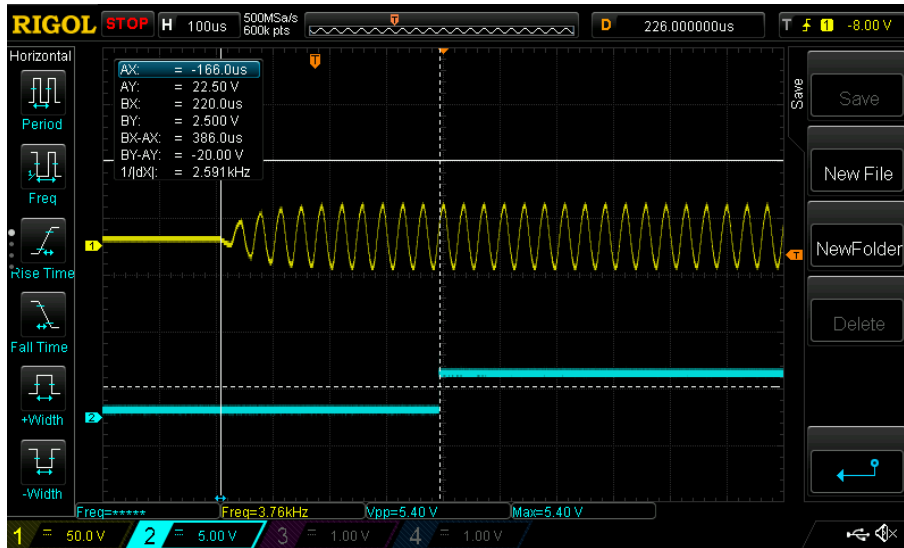


Figure 4-5: BFSK demodulation receiver and transmission signal delay in water tank testing setup

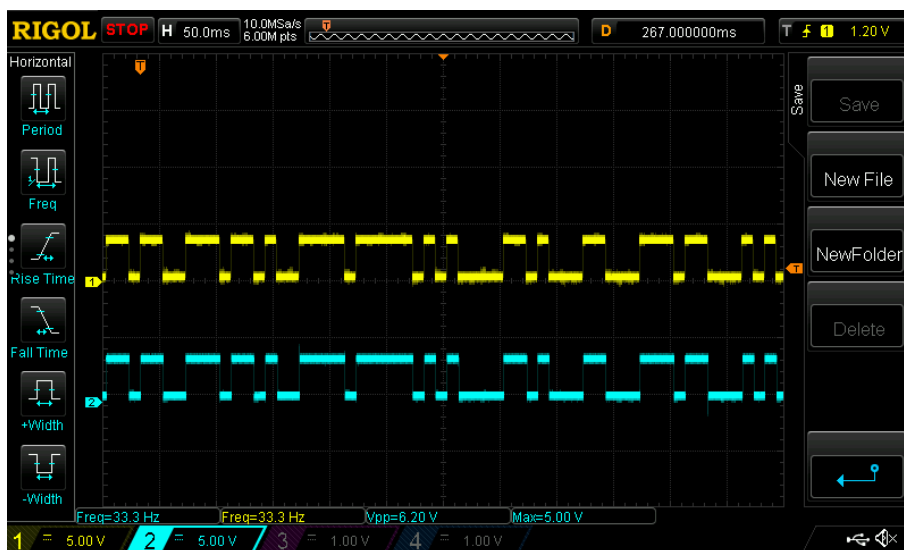


Figure 4-6: The yellow trace is the transmission signal at 100 bits per second. The blue trace is the decoding BFSK output

In the water tank testing setup, the OpenModem with the BFSK modulation scheme was able to successfully transmit and receive signal at 100 bits per second with accuracy greater than 99 %.

4.2.2 DBPSK

We measured the analog voltage across the transducer during DBPSK transmission and receiving. A 8-bit pattern [0 1 1 0 0 1 0 1] was transmitted. The transmission bit rate is set at 200hz, 5ms bit duration. From the amplified analog received signal, we can see the effect of ringing and normal mode vibration at the end of the transmission. There is also inter symbol interference and delay in phase shift in the receiver signal. The power spectrum of the receiver signal showed a distinctive peak at the carrier frequency 24kHz.

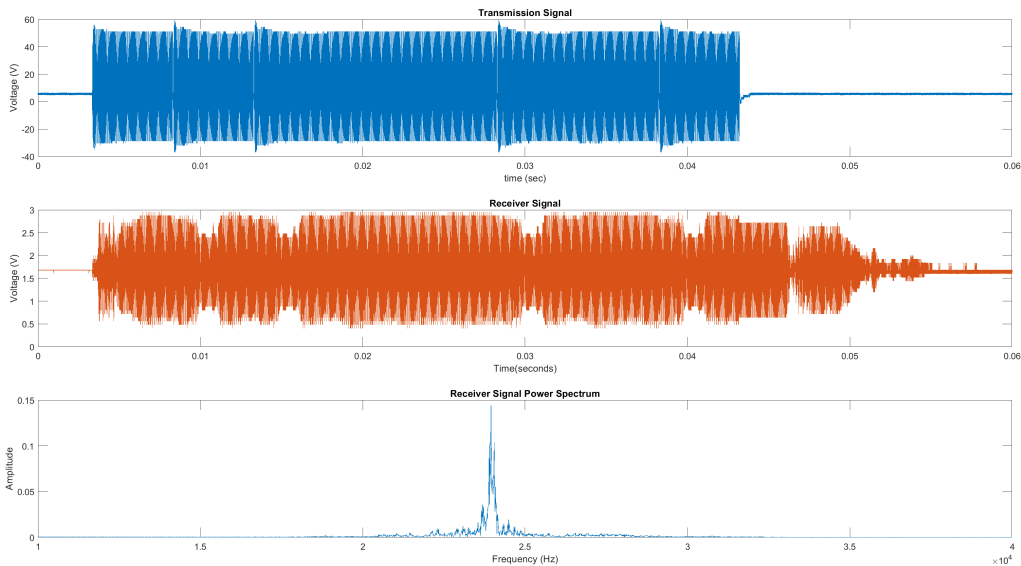


Figure 4-7: DBPSK modulated analog signals of transmission and receiving modem

To verify the operation of DBPSK digital decoding, we sent a 100 bits package at 100 bits per second. The start bit is set up as two-bit duration, one with 0° phase shift, one with 180° phase shift. The receiver modem was able to successfully demodulate the transmitted package.

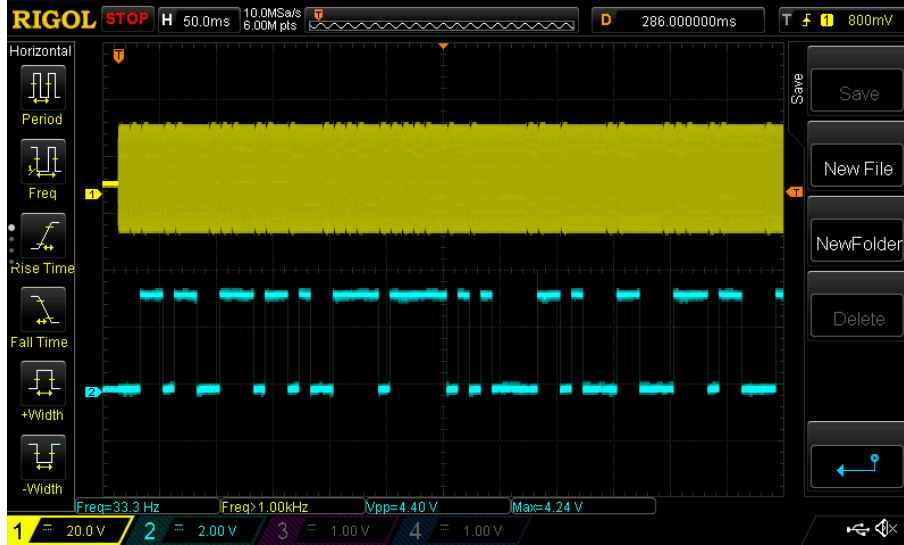


Figure 4-8: Yellow trace is the transmission analog signal at 100 bits per second, Blue trace is the decoding DBPSK output

The transmission delay with the DBPSK demodulation is the sum of acoustic wave travel time, integration time, and one starting bit duration. The DBPSK modulation signal delay can be calculated by the formula below, D is the transmission distance in meter, N is the Goertzel Algorithm bin size, v is the speed of acoustic wave in water, and t_{bit} is the duration of 1 bit.

$$Delay_{DBPSK} = \frac{D}{v} + \frac{N}{f_{sample}} + t_{bit}$$

The estimated transmission delay is $0.333ms + 100samples/100kHz + 10ms = 10.433ms$. The measured transmission delay is 10.84ms. At longer transmission distance, the delay is dominated by time it takes for the acoustic wave to travel between the modems.

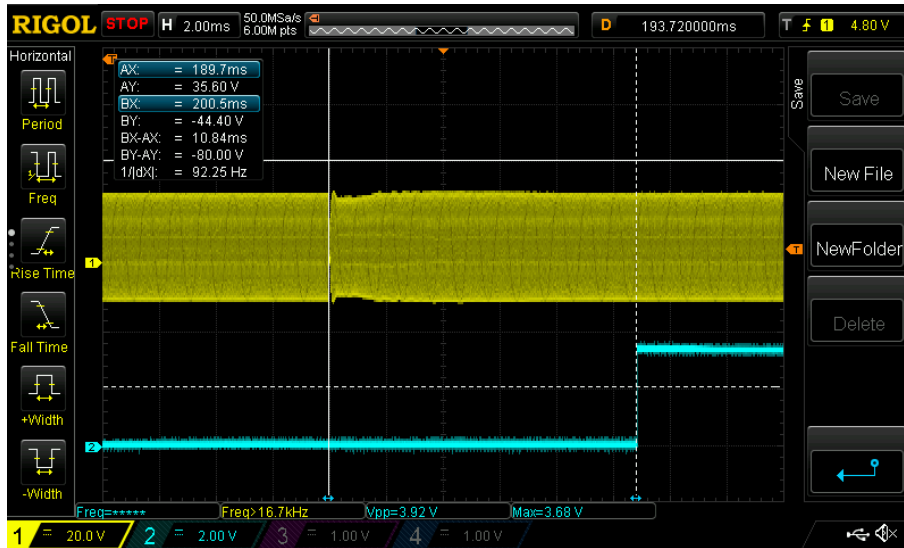


Figure 4-9: Signal Delay



Figure 4-10: The yellow trace is the transmission digital signal at 100 bits per second, and the blue trace is the decoded DBPSK output

In the tank testing setup, the OpenModem was able to transmit and receive DBPSK modulated codes at 100 bits per second with accuracy greater than 99%.

4.3 Power Analysis

The Openmodem battery pack supplies 40 watt-hours of power. Quiescent power draw, Teensy 4.0 at idle mode, is average 60mA at 12V, 720mW. The modem during receiver mode draws on average 70mA at 12V, 840mW. During transmission, the Openmodem draws on average 100mA at 12V, 1.2W. The average power across piezo ceramic transducer is 22mA at 12V, 264mW, with peak current draw at 195mA and peak power draw at 2.35W.

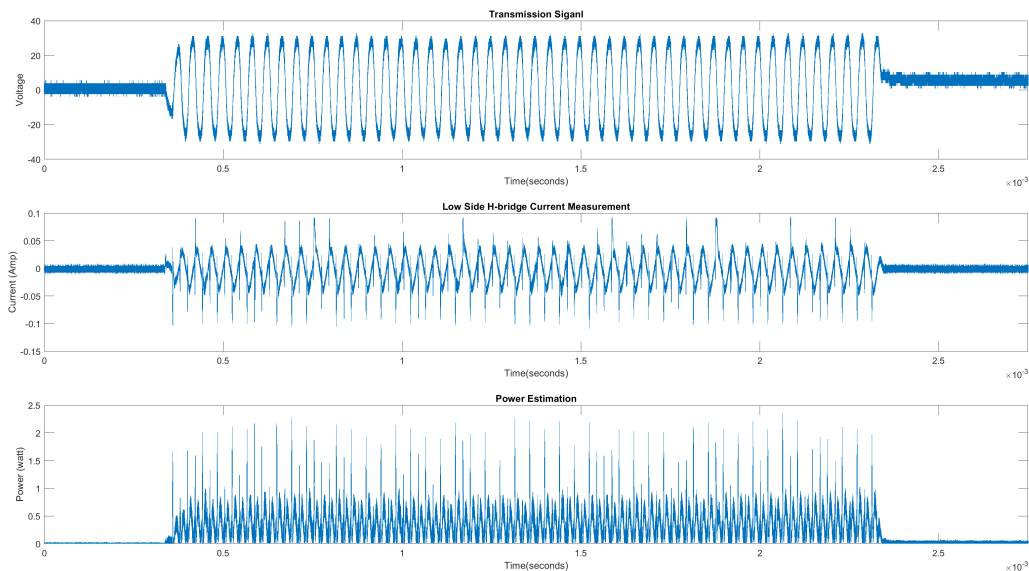


Figure 4-11: Measured voltage, current and power draw across piezo transducer during transmission at 24kHz

For a pure receiving operation, the OpenModem's maximum operating time is 47.8 hours. For a pure transmission operation, the maximum operating time is 33.3 hours. For example, during an infield deployment, the OpenModem is operating at 1 TX and 1 RX operations per hour. Each operation is transmitting and receiving a package of 64 8-bit codes at 100 to 2000 bits per second.

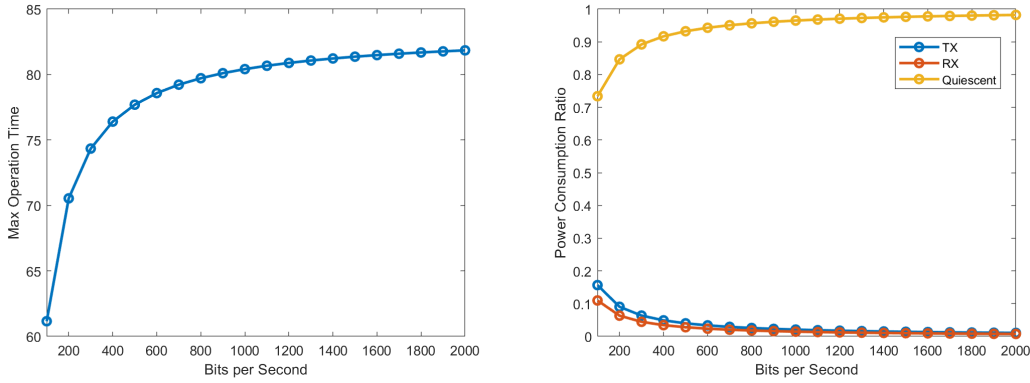


Figure 4-12: Right: Maximum OpenModem operation time at different bit rate. Left: The power consumption ratios of transmission operation, receiving operation and quiescent state at different bit rate.

At higher bit rates, the transmission and receiving operations are more efficient. The maximum operation time starts to plateau at around 600 bits per second. At 1 TX and 1 RX operations per hour, the dominating power consumption source is from the quiescent state power draw.

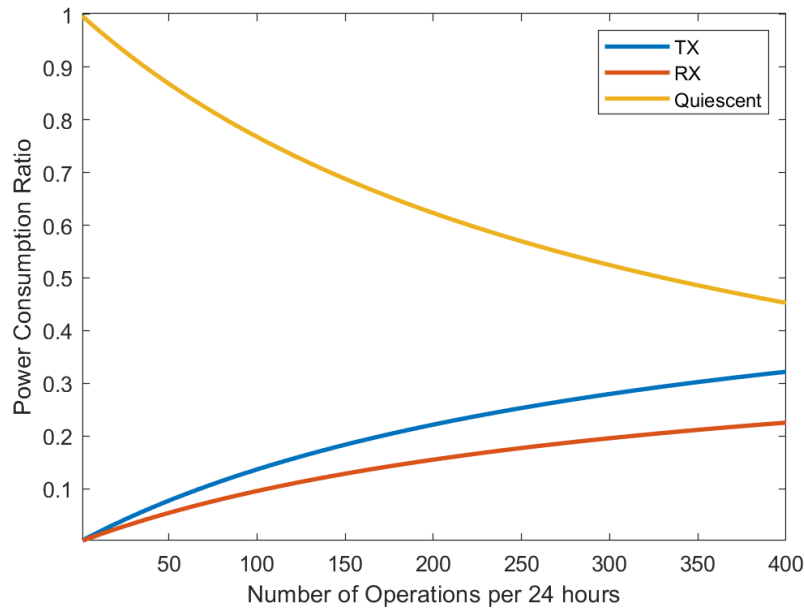


Figure 4-13: OpenModem transmission, receive and quiescent power consumption ratio at different number of operations (500 bits per second) per 24 hours

Different deployment goals and conditions require different operation rates. At a low operation rate, the quiescent power draw dominates the total power consumption.

At a higher operation rate, the transmission power consumption starts to dominate. Low operation mode (<10 operations per hour) is likely the most common development mode for the OpenModem. Therefore cutting down the quiescent power consumption is essential for increasing battery life. At higher operation mode, increasing the efficiency of transmission operation will be essential for increasing battery life.

4.4 Bill of Material

The Bill of Material (BOM) for OpenModem at low volume production (LV), <10, is \$191.80, and at high volume production (HV), >1000, is \$83.295. The BOM cost does not include shipping, storage, machining, and assembling cost. Potting of the transducer could be high labor cost, if the part can not be outsourced effectively.

At LV production, BOM is evenly spread amongst the 6 categories, transmission, receiver, MCU, power supply, piezo transducer, and housing. At HV production, the total cost decreased by almost 50%. The more expensive line items are the Teensy 4.0 and the 25kHz piezoceramic. By designing and embedding a microcontroller chip onboard instead of using the Teensy 4.0 development board, we can easily cut down the MCU BOM to \$5. By switching to a higher frequency piezoceramic transducer, or finding a reliable piezoceramic manufacturing house, we can reduce the piezo transducer BOM to \$5. With the adjustments listed above, the HV BOM cost for a stand-alone OpenModem is around \$60. The HV BOM cost for an OpenModem with an external 12V power supply, for example, when attached to an underwater remote operated vehicle, eliminates the needs for internal batteries. The HV BOM cost is further reduced to around \$50. Design for manufacturing could likely reduce the BOM cost even further.

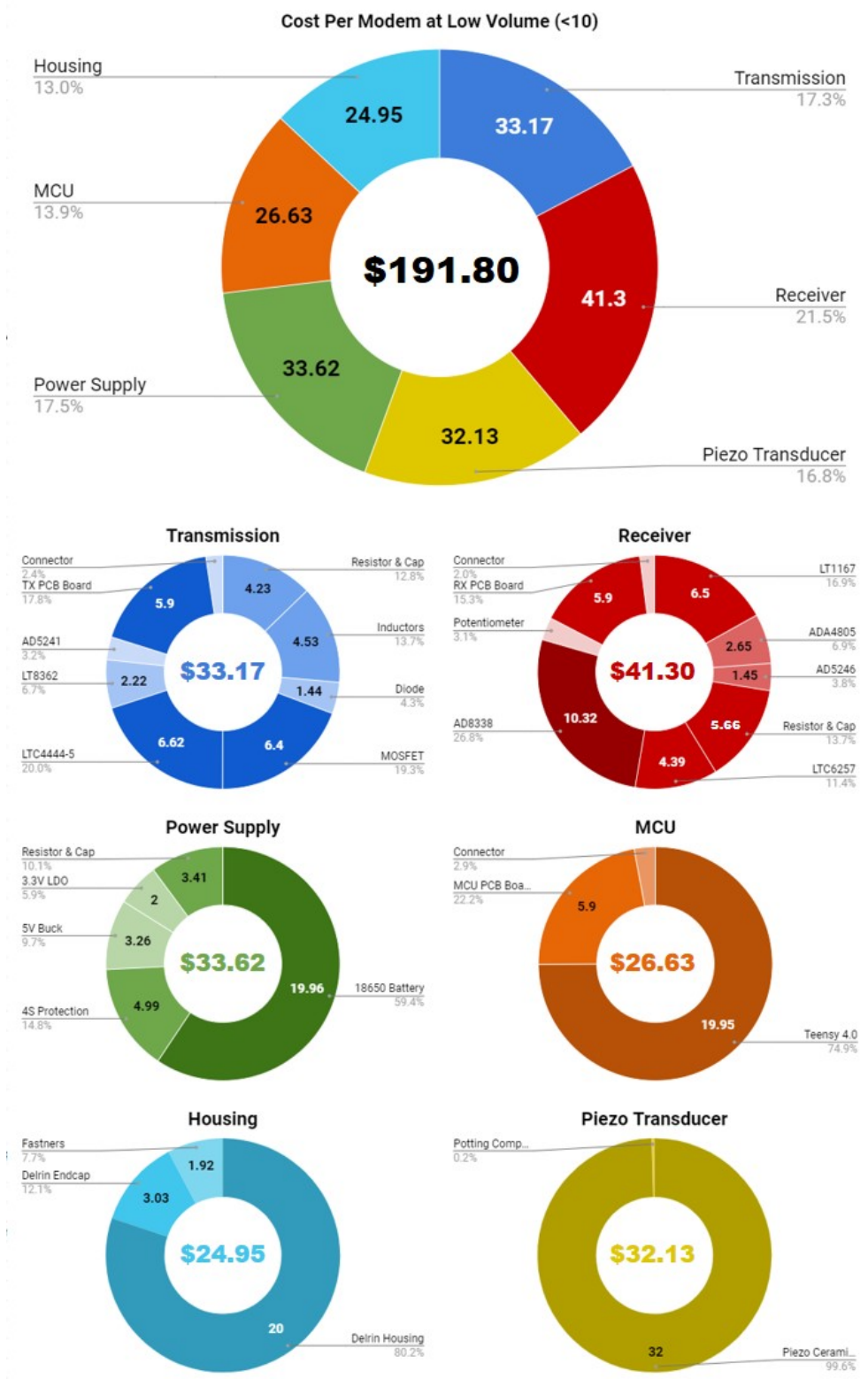


Figure 4-14: OpenModem bill of material breakdown at low volume production (<10)

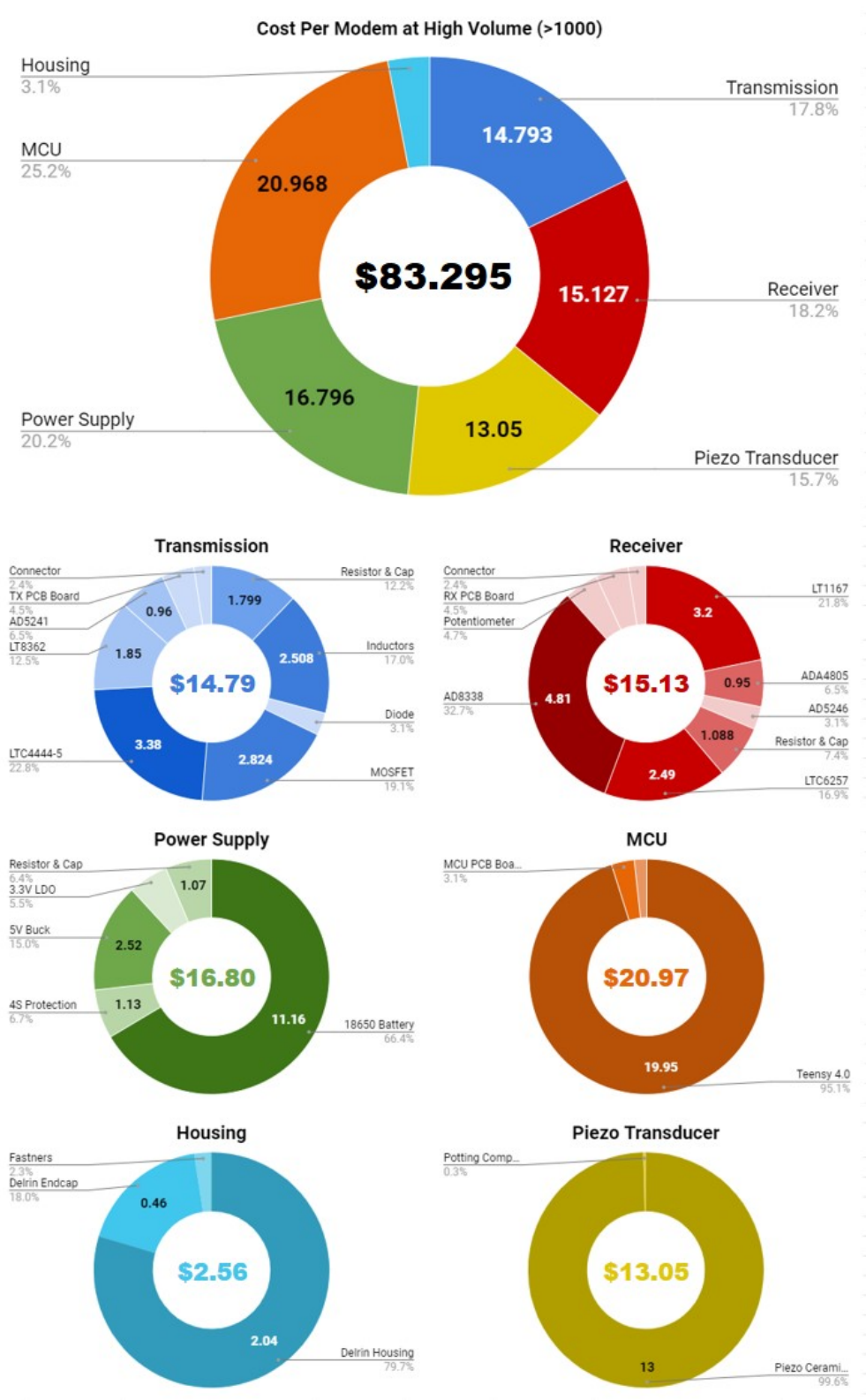


Figure 4-15: OpenModem bill of material breakdown at high volume production (>1000)

Chapter 5

Next Steps

This thesis covers the current design and evaluation of the OpenModem, a low-cost, scalable, and modular underwater acoustic modem. The OpenModem is an open-source and on-going project. The ultimate goal for the OpenModem project is real-world large scale deployment. There is still a continuous effort to drive down the cost and improve the performance and efficiency of the OpenModem design.

As an on-going project, the OpenModem project is currently documented and further updated on <https://futureocean.pubpub.org/>, which includes links to code, CAD drawing, and more. The core modem design can be integrated into underwater sensor devices, underwater vehicles, and more.

5.1 Hardware Consideration

Wake-up Circuit A well-designed wake-up circuit with μW power draw can decrease the quiescent power draw and significantly improve the battery life of the OpenModem at low operation mode. The wake-up circuit allows the MCU unit to sleep until a predetermined wake-up signal is received. There is a range of existing low-frequency wake-up receiver ICs (AS3993, MAX2153) that draws less than $10\mu\text{A}$ at 5V . The design of the wake-up circuit requires high sensitivity at low power consumption. Energy detection is on the most common wake-up circuit architectures [53].

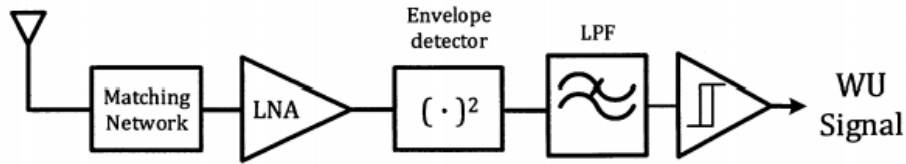


Figure 5-1: Energy detection wake-up circuit block diagram

Embedded MCU Chip Instead of using the Teensy 4.0 development board, we can directly embed a cheaper and low power microcontroller such as the STM32F4 or the MSP432 series. The Teensy development board, however, has a large developer community and a well-documented help forum. Switching to an embedded MCU IC, we need to take the trade-off between costs, ease of development, and performance into consideration.

5.2 Software Considerations

Improve Bit Error Rate Performance The transmission power control using the SEPIC converter is implemented. An adaptive power control algorithm can be implemented to optimize the transmission rate and accuracy in a noisy environment. In addition, an computationally effective adaptive channel equalization algorithm can improve the bit error rate in a highly multipath and non-static environment [54]. We can further improve bit error rate performance by using error correction code, such as the Gold Code or Walsh Code, which allows for code recovery [55].

Modulation Schemes For our current version, we implemented and tested the BFSK and the DBPSK modulation. Low hang fruits are M-FSK and M-DPSK modulations scheme, for a higher bit rate. Higher bit-rate is more power efficient at a higher operational frequency when TX and RX power consumption starts to dominate. Additional modulation schemes worth exploring include but not limited to orthogonal frequency-division multiplexing, quadrature amplitude modulation, and more [52].

JANUS Protocol Currently, only the physical communication layer is imple-

mented. NATO established an open-to-public digital underwater communications standard, JANUS, a simple multiple-access acoustic protocol. JANUS enables open, multi-device, collaborative communication underwater [56]. It is robust against communication errors, can be used as a means of remote control in case of unexpected behaviors. The protocol defines a procedure for handshaking, synchronization, and 80bps data transmission using 56-bit packets. Once synchronized, the systems can then switch to a different frequency or protocol. It also provides redundancy checking for reducing errors caused by interference and Doppler effect.

5.3 Design Variations

Underwater Wireless Sensor module The OpenModem can be used as an underwater wireless sensor module by connecting different sensors onto the modem. The OpenModem can provide power, data logging, and wireless data transfer for low-power sensors.

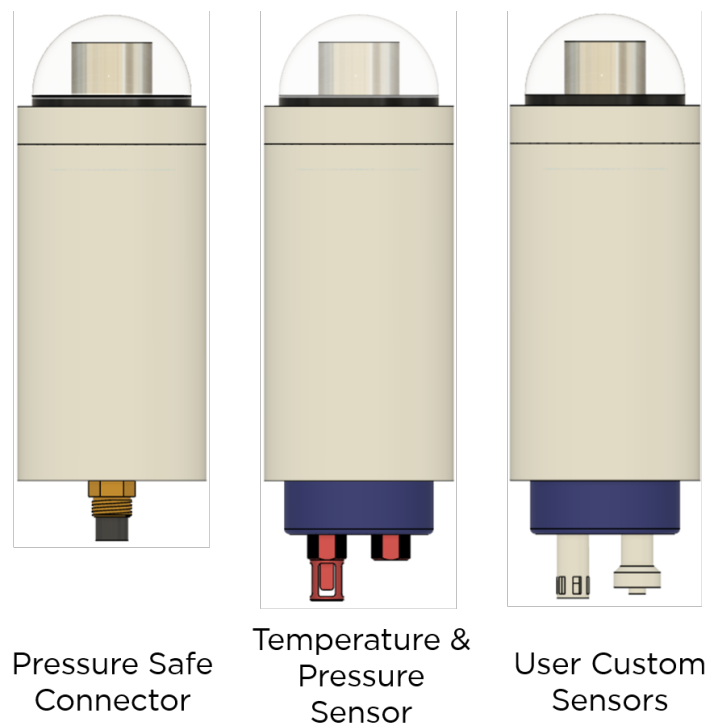


Figure 5-2: OpenModem with modular custom sensor and connector attachments

Pico OpenModem The Pico OpenModem is a concept of a minimal version of the OpenModem design with no battery, no housing, fully potted with a simple serial port output, and power connections. It can be a small and inexpensive wireless communication module for an existing system or platform. It can be used as a remote control for underwater ROV, or part of a simple wireless alert system on monitoring buoys.

Different Carrier Frequency The current OpenModem design operates on a narrow bandwidth of around 25kHz. The design can be adapted to higher carrier frequencies (150kHz to 2Mhz). At higher transmission frequencies, we can achieve a higher bit-rate. A higher frequency signal suffers stronger attenuation, therefore the transmission distance is shorter. However, the stronger attenuation at the same time alleviates multipath interference.

Piezoceramics with higher mechanical resonants are smaller in size. The reported static capacitance and resonant impedance in-air are shown below. The tables below are some recommended transmission and receiver hardware values and constrain for the different piezoceramic transducers. As shown in chapter 2, the electric characteristic of the piezoceramic will change when it is potted and submerged in water. The recommended values and constrains are estimated based on the reported piezoceramic values in-air.

Piezo transducer

Model	SMC0604T6121 (cylinder)	WuHan Piezohannas PZT 5A (hemisphere)	WuHan Piezohannas PZT 5A (hemisphere)	SMC3015T4410 (cylinder)	SMSF20C30F21 (partial hemisphere)
Mechanical Resonant Frequency (kHz)	155	188	390	520	2000
Resonant Impedance (ohm)	150	15	10	90	5
Static capacitance @ 1kHz (nF)	2.5	1.5	0.55	0.35	3.6

The impedance matching inductor values are tuned to match the impedance of

the piezoceramic near its mechanical resonance. A high total parasitic resistance in the TX circuit can affect the power efficiency and introduce RC time constant. The main sources of parasitic resistance come from the inductor's resistance ($\tilde{1}\text{m}\Omega$) and the MOSFET($\tilde{15}\text{m}\Omega$) drain-source resistance. The recommended maximum parasitic resistance value minimizes the power lost to heat to 1%, and the RC cutoff frequency is well above the carrier frequency. The parasitic capacitance with the impedance-matching inductor will cause additional ringing and noise. The main sources of parasitic capacitance come from the TX diodes ($<10\text{pF}$) and the MOSFET output capacitance ($\tilde{100}\text{pF}$). The recommended maximum allowable parasitic capacitance value keeps the $LC_{parasitic}$ frequency well above the carrier frequency. Switching rise time depends on the MOSFET's rise time, its input capacitance, and the MOSFET driver's current capability. The maximum allowable switching rise time is within 20% of the carrier half period. Besides the impedance-matching inductor, the current MOSFET, diode, and gate driver choices are within the limitations for the higher frequency piezoceramic transducers listed.

Transmission

Tuned Electrical Resonant Frequency (kHz)	150	180	380	500	2000
Inductor value (uH)	450	521	319	289	1.8
Max. Parasitic Resistance (ohm)	1.5	0.15	0.1	0.9	0.05
Max. Parasitic capacitance (pF)	150	100	70	50	100
Max. switching rise time (nS)	1333	1111	526	400	100
Current draw @ (12V) (mA)	79	792	1188	132	2376
Parasitic LC ringing (kHz)	612	697	1065	1323	12000
RC cutoff frequency (MHz)	42	707	2893	505	884
Power Lost (%)	1.0	1.0	1.0	1.0	1.0

For the receiver circuit, we want to make sure the amplifier's bandwidth at least equal to the carrier frequency, so the signal isn't attenuated. The bandwidth of the LTC1167 is 1MHz. 2MHz transmission signal will be attenuated. Recommended InAmp replacement for 2MHz carrier frequency is AD8421, a low power, low cost, and low noise instrumentation amplifier, with 100x gain at 2MHz. AD8421 operates at 5V instead of 3.3V. The AGC amplifier bandwidth should at least be 10x greater than the carrier frequency, so the signal can be amplified. The current AGC amp, AD8338 bandwidth is at 18MHz. However, the AGC attack time and recovery time might not be fast enough at a higher bit-rate. The alternative is to roll-your-own AGC amplifier design with shorter integration time, or use programmable gain control with digital feedback from the microcontroller.

At a higher frequency power transmission, the RX diode's switching speed needs to be fast enough to block the high voltage signal. Following the Nyquist-Shannon sampling theorem, the minimal sampling frequency is at least twice the carrier frequency.

The Teensy 4.0 on-chip ADC max sampling rate is 1MHz. For $>500\text{kHz}$ carrier frequency, we recommend using high-speed external ADC, such as ADC1175, 20MHz ADC with 7.5 effective bits, cost \$1.32 at scale. Alternatively, we could switch out the Teensy 4.0 to the STM32F446RCT6, a Cortex-M4 180MHz MCU with 7.2MHz 8-bits ADC.

Receiver and Processor

Min. InAmp & Bandpass filter bandwidth (kHz)	150	180	380	500	2000
AGC (bandwidth)	1500	1800	3800	5000	20000
Max. RX diode switching speed (nS)	133	111	53	40	10
Minimal ADC Sampling Rate (kHz)	310	376	780	1040	4000

5.4 Biological and Environmental Considerations

It is unavoidable that the deployment of the underwater modem will have effects on the environment and the surrounding marine organism. Microorganisms will start to accumulate on the surface of the modem, disrupting the signal. Marine organisms use sound to communicate, navigate, and feed. We want to avoid or minimally corrupt the marine life sound with the modem's acoustic transmission [57]. The deployment method should be adapted to minimal impact on the environment. For example, for coral reef monitoring, care must be paid to minimize physical interference.

Appendix A

Bill of Material

Transmission Board - Switching Power Amplifier							
Part	Manufacturer	Part Number	Number of Units	Unit of Price (\$ per 1)	Cost (\$)	Unit of Price (\$ per 1000)	Cost (\$)
Current Sense Resistor	Yageo	PE2010FKKE070R1L	1	0.73	0.73	0.175	0.175
Ceramic Capacitors	TDK		4	0.15	0.6	0.05	0.2
Inductors	Bourns	SRR1260A-102K	2	1.07	2.14	0.489	0.978
Diode	ON Semiconductor	MMDL770T1G	2	0.24	0.48	0.047	0.094
N-Channel MOSFET	STMicroelectronics	STD70N10FA	4	1.6	6.4	0.706	2.824
LTC4444-5	Analog Devices	LTC4444EMSS8E-5	2	3.31	6.62	1.69	3.38
Transmission Board - SEPIC Converter							
Part	Manufacturer	Part Number	Number of Units	Unit of Price (\$ per 1)	Cost (\$)	Unit of Price (\$ per 1000)	Cost (\$)
LT8362	Analog Devices	LT8362EED	1	2.22	2.22	1.85	1.85
AD5241	Analog Devices	AD5241BRUZ10	1	1.05	1.05	0.96	0.96
Inductors	Würth Elektronik	744878004	1	2.39	2.39	1.53	1.53
Thick Film Resistors	Yageo		6	0.15	0.9	0.064	0.384
Ceramic Capacitors	TDK		10	0.2	2	0.104	1.04
Diode	Diodes Incorporated	DLFSS260-7	2	0.48	0.96	0.18	0.36
TX PCB Board	PCBway	Custom	1	5.9	5.9	0.66	0.66
Connector	Samtec	DW-02-15-T-D-400	2	0.39	0.78	0.179	0.358

Receiver Board - Diode Protection

Part	Manufacturer	Part Number	Number of Units	Unit of Price (\$ per 1)	Cost (\$)	Unit of Price (\$ per 1000)	Cost (\$)
Thick Film Resistors Diodes	Yageo On Semiconductor	NSD914XV2T1G	2	0.1	0.2	0.005	0.01
			8	0.33	2.64	0.052	0.416

Receiver Board - Instrumentation Amplifier

Part	Manufacturer	Part Number	Number of Units	Unit of Price (\$ per 1)	Cost (\$)	Unit of Price (\$ per 1000)	Cost (\$)
Thick Film Resistors Ceramic Capacitors	Analog Device Analog Device Analog Device Yageo TDK	LT1167CS8PBF ADA4805-1ARJZ-R7 AD5246BKSZ100-R7	1	6.5	6.5	3.2	3.2
			1	2.65	2.65	0.95	0.95
			1	1.45	1.45	0.46	0.46
			5	0.1	0.5	0.005	0.025
			3	0.2	0.6	0.1	0.3

Receiver Board - Bandpass Filter

Part	Manufacturer	Part Number	Number of Units	Unit of Price (\$ per 1)	Cost (\$)	Unit of Price (\$ per 1000)	Cost (\$)
LTC6257 1% Thick Film Resistors 1% Ceramic Capacitors	Analog Device Yageo Murata Electronics	LTC6257CMS	1	4.39	4.39	2.49	2.49
			12	0.1	1.2	0.006	0.072
			9	0.24	2.16	0.059	0.531

Receiver Board - Auto Gain Control Amplifier

Part	Manufacturer	Part Number	Number of Units	Unit of Price (\$ per 1)	Cost (\$)	Unit of Price (\$ per 1000)	Cost (\$)
10Kohm Potentiometer Trimmer Thick Film Resistors Ceramic Capacitors RX PCB Board Board to Board Connector	Analog Device TT Electronics Yageo Murata Electronics PCBway Samtec	AD838ACPZ-R7 22AR10KLFTR Custom DW-02-15-T-D-400	1	10.32	10.32	4.81	4.81
			1	1.21	1.21	0.685	0.685
			2	0.1	0.2	0.005	0.01
			3	0.2	0.6	0.05	0.15
			1	5.9	5.9	0.66	0.66
			2	0.39	0.78	0.179	0.358

Piezo Ceramic Transducer									
Part	Manufacturer	Part Number	Number of Units	Unit of Price (\$ per I)	Cost (\$)	Unit of Price (\$ per 1000)	Cost (\$)		
Piezo Ceramic Transducer	STENiNC	SMC3831T25111	1	32	32	13	13		
Piezo Ceramic Transducer	OURS UltraSonic	ARS-YGJP-P5-1	1	0.08	0.08	0.04	0.04		
Potting Compound	BIB Enterprises	WC-565 A/B	1	0.05	0.05	0.01	0.01		
PU Jacket Cable			1						
Pressure Housing									
Part	Source	Part Number	Number of Units	Unit of Price (\$ per I)	Cost (\$)	Unit of Price (\$ per 1000)	Cost (\$)		
Delrin Housing	ePlastic	90mm Diameter Rod	1	20	20		0		
Delrin Endcap	ePlastic	90mm Diameter Rod	1	3.03	3.03		0		
Delrin Housing	Dongguan Lishi Industrial	90mm Diameter Rod	1		0	2.04	2.04		
Delrin Endcap	Dongguan Lishi Industrial	90mm Diameter Rod	1		0	0.46	0.46		
Fasteners	McMaster-Carr	316 M3 25mm	6	0.32	1.92	0.01	0.06		
O-ring	McMaster-Carr	146 70A	1	0.002	0.002	0.001	0.001		
Microcontroller									
Part	Manufacturer	Part Number	Number of Units	Unit of Price (\$ per I)	Cost (\$)	Unit of Price (\$ per 1000)	Cost (\$)		
Teensy 4.0	PJRC	Teensy 4.0	1	19.95	19.95	19.95	19.95		
Transmission PCB Board	PCBWay	Custom	1	5.9	5.9	0.66	0.66		
Board to Board Connector	Santec	DW-02-15-T-D-400	2	0.39	0.78	0.179	0.358		
Power Supply									
Part	Manufacturer	Part Number	Number of Units	Unit of Price (\$ per I)	Cost (\$)	Unit of Price (\$ per 1000)	Cost (\$)		
18650 Battery	LG	INR18650 MJI 350mAh	4	4.99	19.96	2.79	11.16		
4s Battery Protection PCB	All Electronics Trading Company	4S 30A Li-ion Protection Board	1	4.99	4.99	1.13	1.13		
5V Buck Converter	RECOM Power	R-78E5.0-1.0	1	3.26	3.26	2.52	2.52		
3.3V Linear Regulator	Texas Instruments	REG1117-3.3	1	2	2	0.916	0.916		
Ceramic Capacitors	Murata Electronics		7	0.2	1.4	0.05	0.35		
Electrolite Capacitor	Panasonic	EEH-ZA1V101V	1	2.01	2.01	0.72	0.72		

Bibliography

- [1] Lisa A. Levin and Nadine L. Bris. The deep ocean under climate change. *Science*, 350(6262):766–768, 2015.
- [2] Jon Copley. Just How Little Do We Know about the Ocean Floor? - Scientific American.
- [3] Lisa A. Levin, Brian J. Bett, Andrew R. Gates, Patrick Heimbach, Bruce M. Howe, Felix Janssen, Andrea McCurdy, Henry A. Ruhl, Paul Snelgrove, Karen I. Stocks, David Bailey, Simone Baumann-Pickering, Chris Beaverson, Mark C. Benfield, David J. Booth, Marina Carreiro-Silva, Ana Colaço, Marie C. Eblé, Ashley M. Fowler, Kristina M. Gjerde, Daniel O. B. Jones, K. Katsumata, Deborah Kelley, Nadine Le Bris, Alan P. Leonardi, Franck Lejzerowicz, Peter I. Macreadie, Dianne McLean, Fred Meitz, Telmo Morato, Amanda Netburn, Jan Pawlowski, Craig R. Smith, Song Sun, Hiroshi Uchida, Michael F. Vardaro, R. Venkatesan, and Robert A. Weller. Global Observing Needs in the Deep Ocean. *Frontiers in Marine Science*, 6(May):1–32, 2019.
- [4] LinkQuest, Inc. LinkQuest.
- [5] AquaSeNt LLC. Technology — Aquatic Sensor Network Technology.
- [6] EvoLogics GmbH. Acoustic Modems | EvoLogics.
- [7] Aquacomm LLC. Aquacomm Underwater Acoustic Modems - Proven and Reliable.
- [8] Teledyne Marine LLC. Teledyne Benthos - Acoustic Releases, Hydrophones & Towed Survey Platforms.
- [9] Trittech International Limited. Micron Modem | Trittech | Outstanding Performance in Underwater Technology.
- [10] Poncela Javier Otero Pablo Zia, Muhammad Yousuf Irfan. State-of-the-Art Underwater Acoustic Communication Modems: Classifications, Analyses and Design Challenges. *Wireless Personal Communications*, May 2020, 2020.
- [11] Mehmet Aydinlik, A. Turan Ozdemir, and Milica Stajanovic. A physical layer implementation on reconfigurable underwater acoustic modem. *Oceans 2008*, pages 1–4, 2008.

- [12] Iuliu Vasilescu, Carrick Detweiler, and Daniela Rus. AquaNodes. page 85, 2007.
- [13] Bridget Benson, Ying Li, Brian Faunce, Kenneth Domond, Don Kimball, Curt Schurgers, and Ryan Kastner. Design of a low-cost underwater acoustic modem. *IEEE Embedded Systems Letters*, 2(3):58–61, 2010.
- [14] Eric Gallimore, Jim Partan, Ian Vaughn, Sandipa Singh, Jon Shusta, and Lee Freitag. The WHOI micromodem-2: A scalable system for acoustic communications and networking. *MTS/IEEE Seattle, OCEANS 2010*, pages 1–7, 2010.
- [15] Antonio Sánchez, Sara Blanc, Pedro Yuste, Angel Perles, and Juan José Serrano. An ultra-low power and flexible acoustic modem design to develop energy-efficient underwater sensor networks. *Sensors (Switzerland)*, 12(6):6837–6856, 2012.
- [16] Gianni Cario, Alessandro Casavola, Marco Lupia, and Claudio Rosace. SeaModem: A low-cost underwater acoustic modem for shallow water communication. *MTS/IEEE OCEANS 2015 - Genova: Discovering Sustainable Ocean Energy for a New World*, 1:1–6, 2015.
- [17] L. M. Brekhovskikh, Yu. P. Lysanov, and Robert T. Beyer. Fundamentals of Ocean Acoustics . *The Journal of the Acoustical Society of America*, 90(6):3382–3383, 1991.
- [18] Salvador Climent, Antonio Sanchez, Juan Vicente Capella, Nirvana Meratnia, and Juan Jose Serrano. Underwater acousticwireless sensor networks: Advances and future trends in physical, MAC and routing layers. *Sensors (Switzerland)*, 14(1):795–833, 2014.
- [19] Edwin Dertien Paul Regtien. *Sensors for Mechatronics (second Edition)*, chapter 9.1.4. Elsevier, 2018.
- [20] R.-M. Guillermic, M. Lanoy, A. Strybulevych, and J.h. Page. A pdms-based broadband acoustic impedance matched material for underwater applications. *Ultrasonics*, 94:152–157, 2019.
- [21] Shawn E Burke and Joseph A. Paradiso. High-resolution piezopolymer acoustic bearing estimator. *Telecommunication RD*, 1996.
- [22] James F. Tressler. *Piezoelectric and Acoustic Materials for Transducer Applications*, chapter Piezoelectric Transducer Designs for Sonar Applications. Springer-Verlag Berlin Heidelberg, 2008.
- [23] David Soares Antonio Arnau Vives. *Piezoelectric Transducers and Applications (Second Edition)*, chapter 1 Fundamentals of Piezoelectricity. Springer-Verlag Berlin Heidelberg, 2008.
- [24] Steminc Piezo Ceramics. Piezo ceramic cylinder 38x31x25mm 25 khz, Jun 2008.

- [25] Robert Urick. *Principles of Underwater Sound 3rd Edition*. Peninsula Publishing, 1996.
- [26] Ricardo Queirós, Pedro Silva Girão, and António Serra. Single-mode piezoelectric ultrasonic transducer equivalent circuit parameter calculations and optimization using experimental data. 09 2005.
- [27] Miguel Alvarado Juarez. *Construction and Testing of Low-Noise Hydrophones*. PhD thesis, Naval Postgraduate School, 2003.
- [28] Paul P.L. Regtien. 9 - acoustic sensors. In Paul P.L. Regtien, editor, *Sensors for Mechatronics*, pages 241 – 274. Elsevier, Oxford, 2012.
- [29] BJB Enterprises, Inc. Wc-565 a/b water clear shore 65 a polyurethane elastomer.
- [30] Andrei Grebennikov and Nathan O. Sokal. Chapter 1 - power-amplifier design principles. In Andrei Grebennikov and Nathan O. Sokal, editors, *Switchmode RF Power Amplifiers*, pages 1 – 53. Newnes, Burlington, 2007.
- [31] Inc. AspenCore. Amplifier classes and the classification of amplifiers, Jun 2019.
- [32] Andrei Grebennikov and Nathan O. Sokal. Chapter 2 - class-d power amplifiers. In Andrei Grebennikov and Nathan O. Sokal, editors, *Switchmode RF Power Amplifiers*, pages 55 – 93. Newnes, Burlington, 2007.
- [33] Linear Technology. *LTC4444-5 High Voltage Synchronous N-Channel MOSFET Driver*, 1 2011. Rev. C.
- [34] ON Semiconductor. *FDD8780 N-Channel PowerTrench MOSFET*, 2006. Rev. 1.1.
- [35] Texas Instruments. *INA240 High- and Low-Side, Bidirectional, Zero-Drift, Current-Sense Amplifier With Enhanced PWM Rejection*, 2016. Rev. B.
- [36] Arjun Prakash. Current sensing in an h-bridge. *Texas Instruments TechNotes*, 6 2018.
- [37] Inc. Analog Devices. Dc/dc controller selection guide. *Analog Devices Technical Document*, 6 2018.
- [38] Analog Devices. *LT8362 Low IQ Boost/SEPIC/ Inverting Converter with 2A, 60V Switch*, 2017. Rev. A.
- [39] Analog Devices. *I2C-Compatible, 256-Position Digital Potentiometers*, 2015. Rev. D.
- [40] Linear Technology. *Single Resistor Gain Programmable, Precision Instrumentation Amplifier*, 2011. Rev. C.

- [41] Analog Devices. *0.2 V/C Offset Drift, 105 MHz Low Power, Low Noise, Rail-to-Rail Amplifiers*, 2014. Rev.B.
- [42] Analog Devices. *128-Position I2C-Compatible Digital Resistor*, 2012. Rev.C.
- [43] Filter design tool: Filter wizard: Analog devices.
- [44] Analog Devices. *Low Power, 18 MHz Variable Gain Amplifier*, 2016. Rev.B.
- [45] PJRC Inc. Teensy 4.0 development board.
- [46] NXP Semiconductors. *IMXRT1060 Data Sheet*, 2020. Rev. 0.2.
- [47] Jervis J. Gennari Howard E. Barnes. A review of pressure-tolerant electronics (pte). *Naval Research Laboratory*, 1976.
- [48] Arnold G. Sharp. *Design Curves for Oceanographic Pressure-Resistant Housings*. Woods Hole Oceanographic Institution, 8 1981. Rev. 1.
- [49] Parker Hannifin Corporation. *O-ring Handbook*, 8 2018. Rev. 1.
- [50] Upamanyu Madhow. *Modulation*, page 7–73. Cambridge University Press, 2008.
- [51] Alan V Oppenheim, John R Buck, and Ronald W Schafer. *Discrete-Time Signal Processing; 2nd ed.* Prentice-Hall signal processing. Prentice-Hall, Upper Saddle River, NJ, 1999.
- [52] Vijay K. Garg and Yih-Chen Wang. 4 - modulation and demodulation technologies. In WAI-KAI CHEN, editor, *The Electrical Engineering Handbook*, pages 971 – 981. Academic Press, Burlington, 2005.
- [53] Mohamed Radwan Abdelhamid. *Ultra Low Power, High Sensitivity Secure Wake-up Receiver for the Internet of Things*. PhD thesis, Massachusetts Institute of Technology, 2017.
- [54] Dariush Kari, Nuri Denizcan Vanli, and Suleyman S. Kozat. Adaptive and efficient nonlinear channel equalization for underwater acoustic communication. *Physical Communication*, 24:83 – 93, 2017.
- [55] C. Chien. *Digital Radio Systems on a Chip: A Systems Approach*. Springer US, 2001.
- [56] J. Potter, J. Alves, D. Green, G. Zappa, I. Nissen, and K. McCoy. The janus underwater communications standard. In *2014 Underwater Communications and Networking (UComms)*, pages 1–4, 2014.
- [57] Christine Erbe, Sarah Marley, Renee Schoeman, Joshua Smith, Leah Trigg, and Clare Embling. The effects of ship noise on marine mammals—a review. *Frontiers in Marine Science*, 6, 10 2019.